UNIVERSITÀ' DEGLI STUDI DI TRIESTE

XXIV CICLO DEL DOTTORATO DI RICERCA IN GEOFISICA DELLA LITOSFERA E GEODINAMICA

COORDINATORE
PROF. PETER SUHADOLC

A Bader's topological approach for the characterization of pressure induced phase transitions

Settore scientifico-disciplinare **GEO 06**

DOTTORANDO
FILIPPO PARISI

TUTORE
PROF. FRANCESCO PRINCIVALLE

ANNO ACCADEMICO 2010 / 2011

Preface

The main purpose of the present Ph.D thesis is to propose a procedure for the characterization of mineralogical phases under non-ambient conditions by exploiting the potentiality of the computational methods and of the Bader's topological analysis of the electron density. In particular, two important phase transitions which affect the geodynamics of the Earth's deep interior, namely the post-spinel and the Mg-perovskite to post-perovskite transitions, have been explored.

Two issues have been addressed: the first is the construction of the equation of state at zero temperature of the involved mineralogical phases and the determination of the stability fields, while the second concerns the investigation of the evolution of the electron arrangement across the pressure induced phase transitions in terms of topology of the electron density.

The thesis has been organized into seven chapters. The first one contains a brief overview of ab-initio computational methods and the Bader's theory. In addition a description of the most important features of the phases investigated is given. In the second chapter the prefixed objectives were described, while the third one contains all the computational details. The equation of state and the stability fields are discussed in Chapter 4, while in Chapter 5 and 6 the results of the topological analysis of the electron density are reported and interpreted in the light of the Catastrophe theory.

Finally, the most important insights provided by all the studies are summarized in Chapter 7.

Chapter 1

Theoretical background

The following paragraphs provide an overview of the ab-initio computational methods, their applications in the investigation of periodic systems and the Bader's theory of 'Atoms in Molecules' (AIM).

Moreover a section is dedicated to the description of the mineralogical phases under investigations, namely the ringwoodite and perovskite structures.

1.1. Ab-initio quantum-mechanical methods

Computational methods provide a convenient approach for the investigation of the minerals behavior under extreme conditions. In particular ab-initio quantum-mechanical methods revealed very useful in this field.

A more detailed overview of the theory can be found in Pisani, 1996; Levine, 1999; Helgaker et al., 2000 and Evarestov, 2007.

The aim of ab-initio computational methods is to calculate the chemical and physical properties of the investigated system without the need for empirical a-priori information. The approach is primarily based on the solutions of the Schrödinger's equation which for a static system can be written as:

$$H\Psi=E\Psi \qquad (1.1)$$

where H is the Hamilton operator, Ψ is the wave function, which, according to the quantum-mechanical principles, contain all the information required to describe a physical system, and E is the energy of the system.

The Hamilton operator is commonly expressed as the sum of operators corresponding to the different energetic terms of the system:

$$\hat{\mathrm{H}} = -\frac{\hbar^2}{2}\sum_{\mathrm{K}=1}^{\mathrm{N}}\frac{1}{\mathrm{M}_k}\nabla_k^2 - \frac{\hbar^2}{2m}\sum_{i=1}^{n}\nabla_i^2 - \sum_{i,k}\frac{\mathrm{Z}_k e^2}{r_{ik}} + \frac{1}{2}\sum_{i,j\neq i}\frac{e^2}{r_{ij}} + \frac{1}{2}\sum_{h,k\neq h}\frac{\mathrm{Z}_h \mathrm{Z}_k e^2}{r_{hk}} \qquad (1.2)$$

where the first two terms correspond to the kinetic energy terms (for nuclei and electrons respectively) and the last three terms to the potential energy (electrons-nuclei, nuclei-electrons and nuclei-nuclei respectively).

In principle, a quantum-mechanical description of a molecular or periodic system should be provided for all the involved particles, that is for all electrons and nuclei. However the Born-Oppenhaimer approximation can be applied in order to separate the motion of the nuclei from the electron motion due to the large difference in mass between the electrons and nuclei. The potential energy surface (PES) is first determined, corresponding to the fundamental level of the electronic subsystem for each given nuclear configuration.

The electronic Hamiltonian reduced to the sum of three terms, namely the kinetic energy of the electrons, the potential energy nuclei-electrons and the inter-electronic potential energy:

$$\hat{\mathrm{H}} = -\frac{\hbar^2}{2m}\sum_{i=1}^{n}\nabla_i^2 - \sum_{i,k}\frac{\mathrm{Z}_k e^2}{r_{ik}} + \frac{1}{2}\sum_{i,j\neq i}\frac{e^2}{r_{ij}} \qquad (1.3)$$

The electronic Schrödinger's equation can be exactly solved only for mono-electronic systems (H, He^+, Li^{2+} …), while for the multi-electronic systems the introduction of approximations are required.

A very useful approximation method is known as the variational method. The underlying theorem of the method is the Ritz theorem, which states that the expectation value of the Hamiltonian, computed with any trial wave function, is always higher or equal than the energy of the ground state.

This is the basis of much of quantum chemistry, including Hartree-Fock theory and density functional theory which have been applied in the present work.

1.1.1. The Hartree-Fock method

The basic idea of Hartree-Fock theory is that, if the electrons would not interact with each other, then the Hamiltonian would be separable, and the total electronic wavefunction describing the motions of N electrons would just be the product of N hydrogen atom wavefunctions:

$$\Psi(r_1, r_{2,\ldots,} r_N) = \varphi_1(r_1)\varphi_2(r_2)\ldots\varphi_N(r_N) \quad (1.4)$$

which is known as a Hartree Product.

While this functional form is fairly convenient, it does not include the condition that the electrons, being fermions, have to satisfy the antisymmetry principle, which states that a wavefunction should be antisymmetric with respect to the interchange of any set of space-spin coordinates. By space-spin coordinates, we mean the product of a spatial function χ and a spin function $\sigma = \alpha$ or β.

The antisymmetry principle can be satisfied by using a wavefunction expressed in the form of a single Slater-determinant of N_{el} spin orbitals, where N_{el} is the number of electrons in the system:

$$\Psi = \frac{1}{\sqrt{N!}} \begin{vmatrix} \chi_1(x_1) & \chi_1(x_1) & \cdots & \chi_N(x_1) \\ \chi_1(x_2) & \chi_2(x_2) & \cdots & \chi_N(x_2) \\ \vdots & \vdots & \ddots & \vdots \\ \chi_1(x_N) & \chi_2(x_N) & \cdots & \chi_N(x_N) \end{vmatrix} \quad (1.5)$$

The better approximate wavefunctions can be obtained by applying the variational theorem to the wavefunction expressed as a Slater-determinant. In particular the spatial function χ, which represent the molecular orbitals, can be expressed as a linear combination of a set of given basis functions (so-called “atomic orbital" basis functions, usually atom-centered Gaussian type functions):

$\chi_i = \Sigma c_i \theta_i$ (1.6)

and it is possible to obtain the better χ_i by minimizing the energy as a function of the coefficients c_i

Using equation (1.6) as a trial solution, an approximate form of the Schrödinger's equation, called Hartree-Fock equations, can be used:

$F_i \chi_i = \varepsilon_i \chi_i$ (1.7)

where εi is the energy eigenvalue associated with orbital χi and Fi is the Fock operator defined as:

$$f(x_1) = h(x_1) + \sum_j J_j(x_1) - K_j(x_1) \quad (1.8)$$

The first term in square brackets in eq.8 is a one-electron term, which can be expressed as:

$$h(i) = -\frac{1}{2}\nabla_i^2 - \sum_A \frac{Z_A}{r_{iA}} \quad (1.9)$$

The second term gives the Coulomb interaction of an electron in spin orbital χ_i with the average charge distribution of the other electrons and is called the Coulomb term, defined as:

$$J_j(x_1) = \int dx_2 \left|\chi_j(x_2)\right|^2 r_{12}^{-1} \tag{1.10}$$

The last term in brackets in eq. (7) is harder to explain and does not have a simple classical analog. It arises from the antisymmetry requirement of the wavefunction. It looks much like the Coulomb term, except that it switches or exchanges spin orbitals χ_i and χ_j and is called exchange term.

The expression of this term is:

$$\sum_{j \neq i} \left[\int dx_2 \chi_j^*(x_2)\chi_i(x_2) r_{12}^{-1}\right] \chi_j(x_1) \tag{1.11}$$

Note that the solutions of equations (8) depend on the orbitals, hence it is necessary to guess some initial orbitals and then refine the guesses iteratively. For this reason, Hartree-Fock is called a self-consistent-field (SCF) approach.

The HF method is quite accurate in predicting the most important features of molecules and solids, and often gives accurate electron densities. However, binding energies are always severely underestimated. The difference between the energy calculated on the basis of the HF method and the exact energy of the system is called the correlation energy. Alternative methods including the electron correlation energy are based on the density functional theory.

1.1.2. Density functional theory (DFT)

The key point of DFT is that it is not necessary to calculate the very complicated complete electronic wavefunction for a full description of the system, but it is sufficient the knowledge of the electron density, $\rho(r)$, a simple function of three spatial coordinates.

Hohenberg and Kohn (Hohenberg and Kohn, 1964) formulated two theorems which are the basis of the DFT method:

1) The electron density determines (within an additive constant) the external potential, i.e. the potential due to the nuclei and therefore determines the total energy and the wavefunction.

   All physical measurable quantities based on the electron density are unique functional of the electronic ground state density alone :

   $$E = E[\rho] \tag{1.12}$$

2) The total energy of a system is variational with respect to the electron density which means that the correct $\rho(r)$ provides the minimum possible energy for the ground state. The total electronic energy can be written as:

   $$E[\rho] = E_{kin}[\rho] + E_{e\text{-}n}[\rho] + E_{e\text{-}e}[\rho] + E_{XC}[\rho] \tag{1.13}$$

   where $E_{kin}[\rho]$ is the kinetic energy, $E_{e\text{-}n}[\rho]$ and $E_{e\text{-}e}[\rho]$ are the potential energy (electrons-nuclei and electrons-electrons respectively) and $E_{XC}[\rho]$ is the so-called exchange-correlation energy, which represent the classical electrostatic energy of interaction between an electron and its exchange-correlation hole $\rho_{XC}(r,r')$. If a reference electron is located at the point r, the exchange-correlation hole shows how much the probability of finding another electron at the point r' is decreased.

The accuracy of DFT calculations largely depends on the appropriateness of the approximations made for the calculation of the E_{XC} term.

The first approximation used was the Local Density Approximation (LDA), either in exchange-only form or with inclusion of correlation effects. The LDA is based upon the theory of the homogeneous electron gas. For this simple system the exchange energy and potential are known exactly, and accurate approximations for the correlation parts are known from analytical parameterizations. The approximation is that a system can locally be described as an electron gas with a density equal to the local density of the system. This assumption seems reliable in systems with slowly varying densities (such as certain metals), but not in molecules where the density changes rapidly.

Another approximations are the Generalized Gradient Approximations (GGAs) that are based upon the theory of the (weakly) inhomogeneous electron gas and take the gradient of the density in addition to the density itself. Very good accuracy is reached for many systems and properties with the GGAs, although cases are known in which also these GGAs give qualitatively incorrect results, because the description of some effects requires an ultra-nonlocal density dependence in the functionals, for which a gradient expansion is insufficient. GGA allow a much improved accuracy in the results for energies and geometries.

The major problem with DFT is that the exact functionals for exchange and correlation are not known and only an approximate expression of these terms can obtained. Bearing in mind that the exchange term is exactly calculated at HF level, better results can be obtained by expressing the exchange part of the energy by including a component of the exact exchange energy calculated from Hartree-Fock theory. Functionals of this type are known as hybrid functionals. A hybrid exchange-correlation functional is usually constructed as a linear combination of the Hartree-Fock exact exchange functional and any

number of exchange and correlation explicit density functionals. The parameters determining the weight of each individual functional are typically specified by fitting the functional's predictions to experimental or accurately calculated thermochemical data. One of the most commonly used versions is B3LYP, which stands for Becke, 3-parameter, Lee-Yang-Parr.

1.1.3. Application to periodic systems

The Hartree-Fock and DFT methods have been designed for molecular systems, but they can be easily applied to periodic systems. In this case, instead of calculating the wavefunction for all electrons in the crystal in the real space, it is possible to consider only the number of electrons within one unit cell, but the Kohn-Sham equations still must be solved for each k-point.

If we assume that electrons can move in the crystal periodic potential it is clear that their wave functions must show the potential periodicity.

It is clear that the "potential periodicity" means that if we transfer an electron from a point **r** to a point **r** + **R**, it will "feel" the same physical environment and the same selfconsistent potential:

$$V(\mathbf{r}+\mathbf{R}) = V(\mathbf{r}) \tag{1.14}$$

According to the Bloch theorem, each crystal orbital in the field of such a periodic potential , is a product of a periodic function and a plane wave:

$$\Psi_k(\mathbf{r}) = u_k(\mathbf{r}) e^{i\mathbf{kr}} \tag{1.15}$$

where u_k is a periodic function which has to satisfy the condition:

$$u_k(\mathbf{r}+\mathbf{R}) = u_k(\mathbf{r}) \tag{1.16}$$

The Bloch function has therefore the following property:

$$\Psi_k(r+R) = e^{ikR}\Psi_k(r) \tag{1.17}$$

It is easy to demonstrate that adding a reciprocal lattice vector:

$$\mathrm{K} = h_1 b_1 + h_2 b_2 + h_3 b_3\,; \quad h_i = 0,\pm1,\pm2,... \tag{1.18}$$

where $\mathbf{b_i}$ is a basic vector of the reciprocal lattice1, to the wave vector **k** of a Bloch function gives the following result:

$$\Psi_{k+K}(r) = \Psi_k(r)e^{iKR} = \Psi_k(r) \tag{1.19}$$

This means that the states with **k** and **k** + **K** are equivalent physically. This in turn means that all physically different vectors **k** are contained in a limited area of the reciprocal lattice vector space.

This limited space is called *the first Brillouin zone* or simply *the Brillouin zone*. The first Brillouin zone contains all the smallest non-equivalent wave vectors. These wave vectors fulfill the condition:

$$-\pi \le ka_i \le +\pi\,; (i = 1,2,3) \tag{1.20}$$

where $\mathbf{a}_i$ is the basic vector of the crystal lattice.

1.1.4. The CRYSTAL software

CRYSTAL is a commercially available quantum mechanical electronic structure package which is able to perform *ab initio* calculations of the ground state energy, electronic wave function and properties of periodic systems, with periodic boundary conditions in 1, 2 or 3 dimensions (polymers, slabs and crystals). The software was jointly developed by the Theoretical Chemistry Group at the University of Torino and the Computational Materials Science Group at CCLRC Daresbury Laboratory (UK).

The CRYSTAL package performs the computation of the electronic structure using either Hartree-Fock or Density Functional theory.

In each case the fundamental approximation made is the expansion of the single particle wave functions ('Crystalline Orbital', CO) as a linear combination of Bloch functions (BF) defined in terms of local functions (hereafter indicated as 'Atomic Orbitals', AOs).

The local functions are, in turn, linear combinations of Gaussian type functions (GTF) whose exponents and coefficients are defined by input. Functions of symmetry s, p, d and f can be used Also available are sp shells (s and p shells, sharing the same set of exponents).

1.2.Bader analysis

In this section we would briefly summarize some basic concepts and definitions of the topological analysis of the electron density by pointing out the connections between the topological features of the electron density distribution, the structural stability of a molecular system and the breaking/formation of chemical bonds. A more detailed overview of the theory can be found in Merli et al. (2011).

The topological analysis of the electron density $\rho(\mathbf{r})$, based upon the theory of atoms in molecules (AIM) developed by Bader (1991) analyzes the curvature of $\rho(\mathbf{r})$ at the so-called critical points (CPs) i.e. points denoted by the position vector $\mathbf{r}_c$ where the gradient field $\nabla\rho(\mathbf{r}) \times n(\mathbf{r}) = 0$, where $\nabla\rho(\mathbf{r})$ is the gradient vector of $\rho(\mathbf{r})$ and $n(\mathbf{r})$ is the unit vector normal to surface.

The critical points are characterized by the values of the three eigenvalues ($\lambda_1,\lambda_2,\lambda_3$) of the Hessian matrix of $\rho(\mathbf{r})$ evaluated at the CP coordinates. The CPs are denoted as (ω,σ) according to their rank, ω, which is the number of nonzero eigenvalues (or curvatures), and their signature, σ, which is the algebraic sum of the signs of the eigenvalues. With relatively few exceptions, the rank of CPs in an equilibrium geometry is equal to 3, since

the CP with $\omega < 3$ (degenerate critical points) are unstable and indicate an incipient change in the topology of the electron density. There are four types of stable CPs depending of the signature values: (3,-3), (3,+3), (3,-1), (3,+1). A (3,-3) critical point is a maximum in $\rho(\mathbf{r})$ which means that the charge density decreases for motion in any direction away from this point. For all atoms but hydrogen it can coincide with the position of a nucleus. A (3,+3) critical point is a minimum and the charge density increases for motion in any direction away from the point. This point is found when several rings form a cage and it is therefore called a "cage" critical point (CCP). As for the (3,-1) critical point, $\rho(\mathbf{r})$ is a maximum in the plane defined by the eigenvectors associated to the negative eigenvalues and a minimum along the third axis, perpendicular to this plane. This point is located between two neighbouring atoms defining a bond between them, and it is therefore called bond critical point (BCP). As for the (3,+1) critical point, the electron density is a minimum in the plane defined by the eigenvectors associated to the positive eigenvalues and a maximum along the third axis, perpendicular to this plane. This point has to be found in the middle of several bonds forming a ring. It is also called a ring critical point (RCP).

At this point it is important to point out that the mechanism of making and breaking of chemical bonds is closely related with changes in the morphology of a molecular charge distribution. In particular, according with the *Palis-Smale's* theorem, (Palis & Smale 1970) two different mechanism of structural instability, both illustrated in terms of the behavior of the molecular charge distribution, exists. The first mechanism consists in the formation of a degenerate critical point, or singularity, in the electronic charge distribution and is called *bifurcation catastrophe*, while the second corresponds to the creation of an unstable intersection of the stable and unstable submanifolds of two neighboring critical points, and is called *conflict catastrophe*.

It should be recalled that, the stable and the unstable manifolds of the CP at $\mathbf{r}_c$ are defined to be the manifolds generated by the eigenvectors of the Hessian matrix of $\mathbf{r}$ at $\mathbf{r}_c$ associated with the negative and positive eigenvalues respectively.

In the light of these definition, the stable and the unstable manifolds of a bond critical point are the interatomic surface and the bond path, while, for a ring critical point, the ring axes and the ring surfaces respectively. As a simple example of transversal and non-transversal intersections we can consider the intersection between the stable manifold of a BCP (surface) and the instable manifold of a RCP (curve). When the curve intersect the surface at some finite number of points we can say that the intersection is transversal and a small change in their relative positions will not affect the intersection. On the contrary, if the curve is tangent to the plane (i.e. if the angle between the curve and the plane is close to 0°) the intersection is called non-transversal and a small change in their positions will result in a drastic change.

1.3.Ringwoodite structure

Ringwoodite (γ-Mg_2SiO_4) is the high pressure stable olivine polymorph, with the spinel structure. The spinel structure is based on a nearly ideal cubic close-packed array of oxygen atoms with tetrahedral (T) and octahedral (M) cavities. One eighth of tetrahedral (T) and one half of octahedral (M) sites filled respectively by Si and Mg cations. Ringwoodite is in the isometric crystal system and has space group $Fd\bar{3}m$.

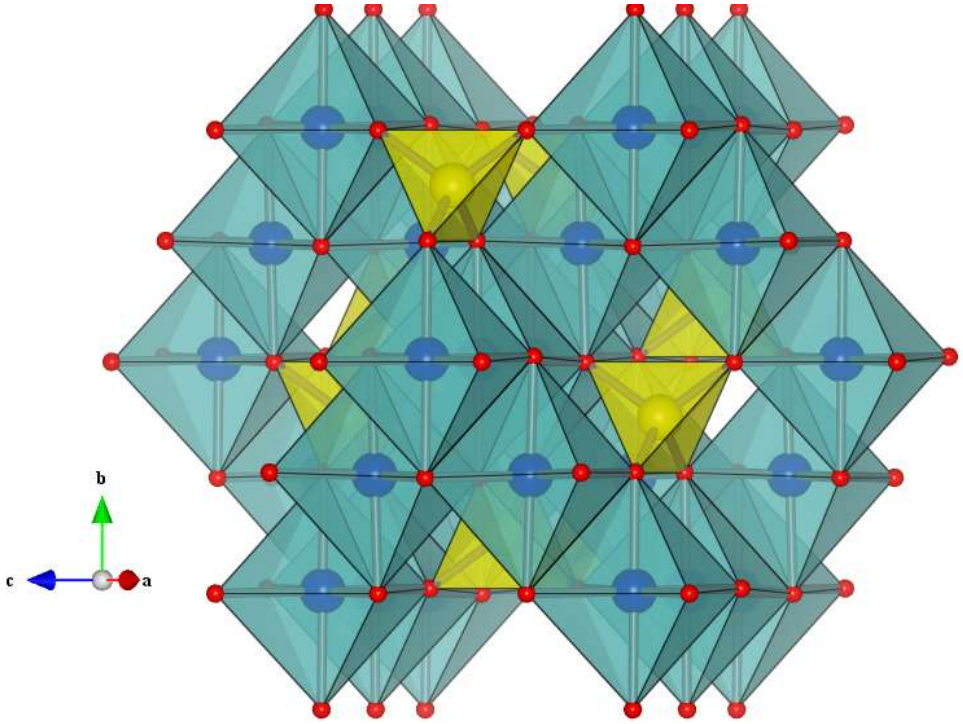

Figure 1.1. γ-Mg_2SiO_4 Ringwoodite structure (SpaceGroup Fd $\bar{3}$ m) with octahedrally coordinated Mg atoms and tetrahedrally coordinated Si atoms.

Ringwoodite is thought to be the most abundant mineral the lower part of the mantel's transition zone (520-660 km depth), which implies that its structural, elastic and thermodynamic properties should affect those of the mantel at this depth.

1.4.Perovskite structure

The perovskite structure, so called for the $CaTiO_3$ perovskite mineral, is the structure of many compounds with the general formula ABX_3. A and B are two cations of very different sizes, and X is an anion that bonds to both. The A atoms are larger than the B atoms.

The ideal structure is cubic with a BO_6 octahedron at each corner forming a cube around the A atom at the centre.

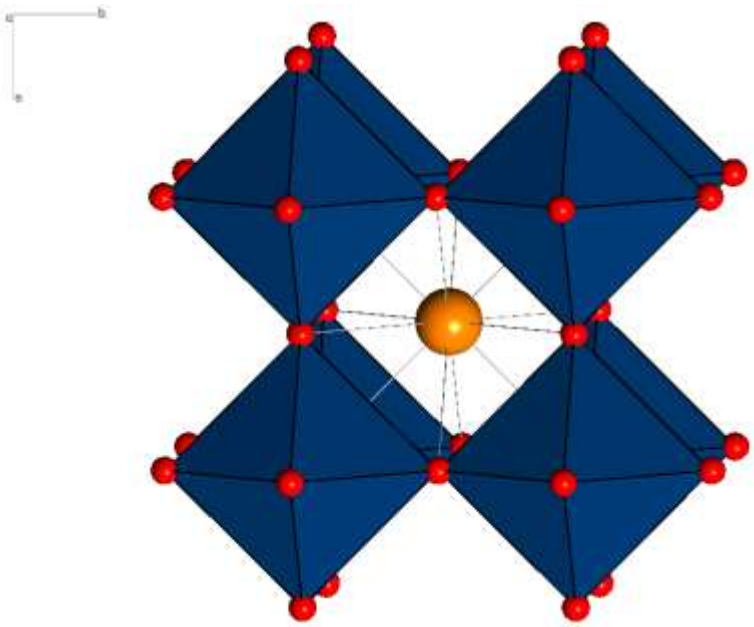

Figure 1.2. Ideal cubic stucture of perovskite where the B atoms form a cube around the A atom at the centre.

The interest in the perovskite structure in mineralogy and geodynamics is due to the fact that a perovskite of composition around $MgSiO_3$ is likely the most abundant phase in the Earth's lower mantle. This means that the most common mineral in the Earth has the perovkite structure.

We studied the $MgSiO_3$ perovskite which structure is composed of an octahedrally coordinated Si atom and a Mg atom in a irregular 8-coordination. The structure would ideally be cubic if the divalent cation were large enough, but the mineral is orthorhombic. The modification of this structure consists in tilting of alternate SiO_6 octahedra in opposite sense.

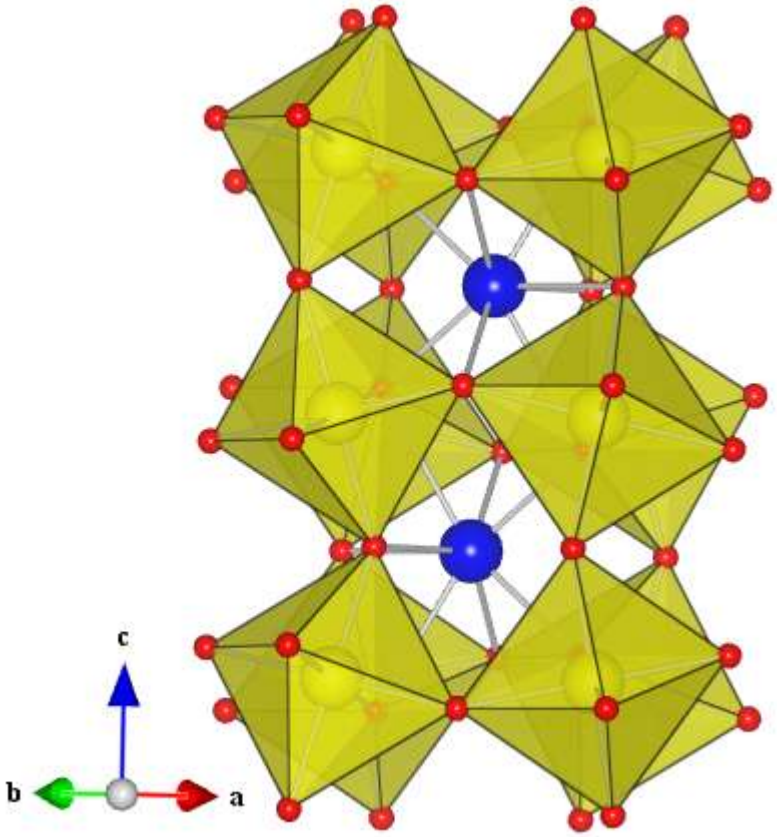

Figure 1.3. $MgSiO_3$-perovskite structure (SpaceGroup Pbnm) with octahedrally coordinated Si atoms and Mg atoms in 8-coordination.

The perovskite structure of $MgSiO_3$ is only stable at very high pressures but has been shown to exist experimentally in apparatus capable of simulating mantle conditions.

Chapter 2

Aims and objectives of the study

Mg_2SiO_4 ringwoodite (γ-spinel phase, space group $Fd\bar{3}m$) is thought to be the most abundant mineral in the lower part of the mantle transition zone (520–660 km depth) (Irifune & Ringwood 1987; Ringwood & Major 1970; Ita & Stixrude 1992), which implies that its structural, elastic and thermodynamic properties should affect those of the mantle at this depth.

According to the most reliable geophysical models, its dissociation into MgO periclase (space group $Fm\bar{3}m$) and $MgSiO_3$ perovskite (space group $Pbnm$), often referred to as *post-spinel* transformation, is believed to be responsible for the 660-km discontinuity that defines the boundary between transition zone and lower mantle (Dziewonski & Anderson 1981; Ringwood 1991; Poirier 1991; Zhao & Anderson 1994; Navrotsky 1994), and would seem to have significant implications for mantle convection processes (Ringwood 1982; Ringwood 1994; Christensen & Yuen 1985; Fukao et al. 1992; Tackley et al. 1993; Van der Hilst 1995). Figure 2.1 shows the approximate volumetric constitution of the mantle.

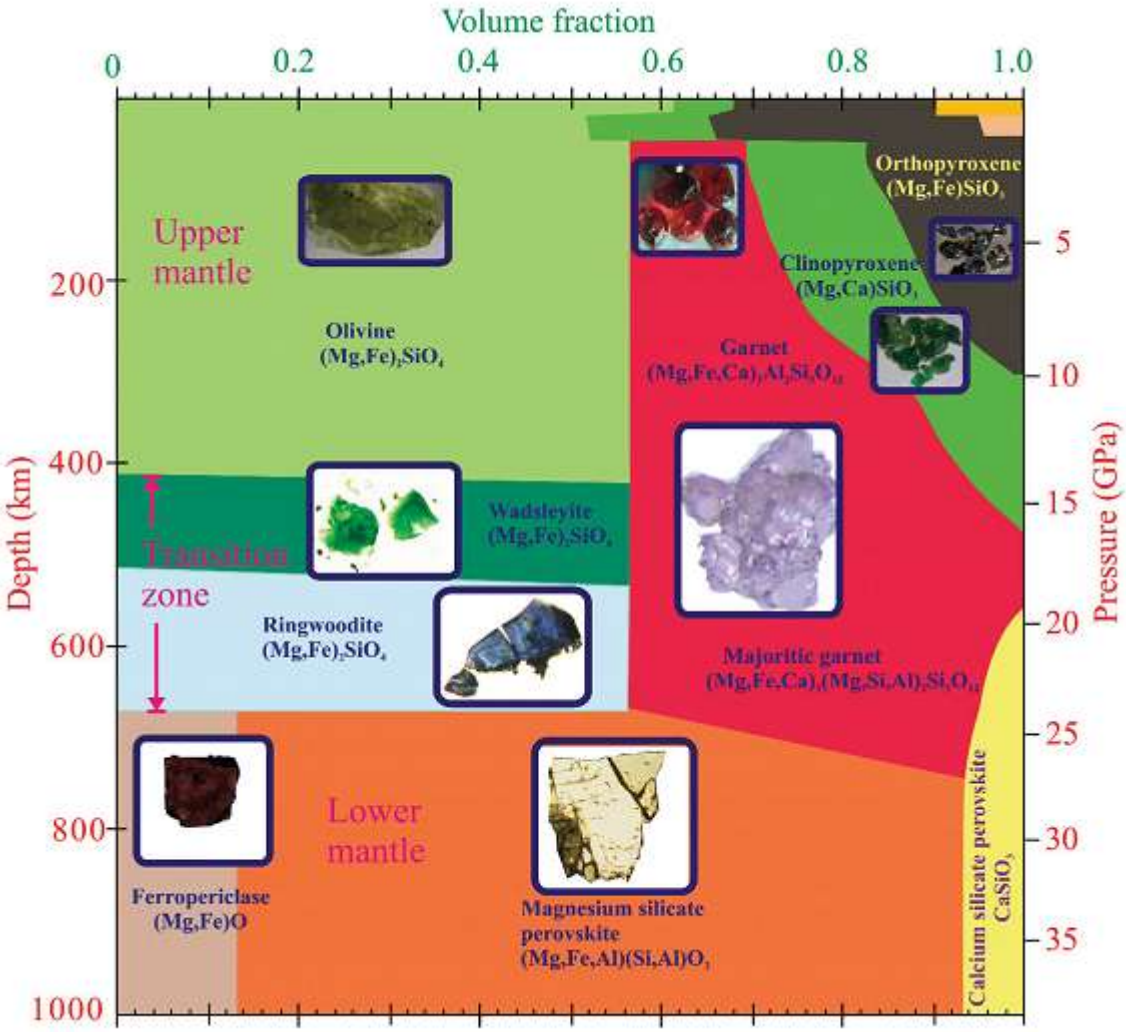

Figure 2.1. The approximate volumetric constitution of the mantle (Frost 2008).

For many petrologists, geophysicist and geodynamicists, the post spinel phase transition is considered, together with the substantial lack of deep earthquakes beyond the 700 km depth, as the main evidence supporting the hypothesis of a two-convection layers in the mantle : the transition zone of the mantle would constitute, in this case, a physical barrier to penetration of the slabs below 660 km. However, not all the scientists agree with this theory, and the debate within the scientific community is still open. In this context, the

total lack of direct observations of the interior of the earth greatly hampers the understanding of the mechanisms influencing the deep geodynamics.

Although the post-spinel transition has been investigated in several works (Irifune et al. 1998; Chudinovskikh & Boehler 2001; Shim et al. 2001, Katsura et al. 2003), the total lack of direct observations of the interior of the Earth greatly hampered the understanding of the mechanisms of the processes influencing the deep geodynamics. Only in the last years, the development of sophisticated experimental techniques rendered feasible the experimental approach to the problem.

The high pressure behavior of natural and synthetic ringwoodite has been studied (Chopelas et al. 1994; Liu et al. 1994; Meng 1994; Kleppe et al. 2002; Liu et al 2002; Zerr et al. 1993; Kleppe et al. 2002b; Koch-Müller et al. 2011) by means of Raman spectroscopy and X-ray diffraction, Brillouin spectroscopy, IR absorption and ultrasonic methods.

However, in the laboratory experiments some results are extremely difficult to obtain either because of the extreme P–T condition or for the very slow reaction kinetics. In this context, it is worth to say that the post-spinel transition is kinetically hindered and requires high temperatures to overcome the high activation energy (Kubo et al. 2002; Yamazaki et al. 1996; Kubo et al. 2009). From recent measurements, the phase boundary pressure between ringwoodite and perovskite was found to be ~22-24GPa in the pressure range 1500-2100 K (Chudinovskikh & Boehler 2001, Katsura et.al. 2003, Shim et al. 2001), while any experimental trial to induce the decomposition process by compressing the ringwoodite phase at room temperature fails resulting in the achievement of a metastable ringwoodite phase (Chopelas et al. 1994; Liu et al. 1994, Meng 1994; Kleppe et al. 2002; Liu et al. 2002; Zerr et al. 1993). The experimental research can be conveniently integrated by computational methods which allow, not only to explore the extreme conditions that

cannot be realized in a laboratory, but also to rule out the experimental problems relating to the slow kinetics.

On the other hand it has to be taken into account that the experimental results are influenced by several factors such water content, impurities and structural disorder, that cannot be easily controlled and whose effects cannot be separated.

On the contrary, the computational approach allows to characterize the system uniquely in terms of the completely anhydrous and totally ordered pure end-member of γ-Mg_2SiO_4, and to consider only the effect of the pressure in the phase transition.

In the light of all these considerations, we decided to undertake the present computational study aimed at obtaining a comprehensive picture of the post-spinel phase transition and an internally consistent set of references to compare with the various experiments. To accomplish this goal the hydrostatic compression of the ringwoodite has been investigated by means of first principle calculations. The equation of state at zero temperature has been constructed and the stability fields have been determined based on the computed enthalpy.

Moreover, aiming at obtaining a deep insight into the nature of the phase transition, the evolution of the electron arrangement in the ringwoodite crystal-structure across the pressure induced phase transition has been investigated in terms of topology of the electron density and a topological approach based on the Catastrophe Theory in the framework of the Bader's theory of 'Atoms in Molecules' (AIM) has been proposed for the first time.

In a second step, in order to test the reliability of the proposed procedure in the characterization of the structural stability of mineralogical phases, the Bader's topological analysis has been performed on the Mg-perovskite structure. The interest in the structural stability of this phase comes from the consideration that the Mg-perovskite is assumed to be the dominant component of the Earth's lower mantle (~ 75%vol, Oganov and Price, 2005) and the transition to the so-called post-perovskite phase can explain the

discontinuity in seismic velocities observed above the core–mantle boundary (the D" discontinuity). Owing to the importance of its contribution to the geophysical properties of the Earth, the structural and elastic behavior of $MgSiO_3$ perovskite have been thoroughly investigated by several authors (e.g. Hama and Suito, 2001 and Deshamps and Trampert, 2004).

Although quite a large amount of data on the perovskite so far exists, its behavior at the extreme conditions of the Earth mantle is still lacking information. This is mainly due to the technical difficulties related to the experimental setup.

As already stated, at extreme conditions, where the experiments lose its accuracy, computational approach can be very helpful in complementing these studies.

Chapter 3

Computational details

The calculations have been performed by means of the ab-initio CRYSTAL09 program (Dovesi et al. 2009) at the HF/DFT level, using Hamiltonians based on the Becke-LYP scheme (Becke 1993) containing hybrid Hartree–Fock/density-functional exchange-correlation terms, which employs the Becke GGA exchange term (Becke 1988) mixed with the exact non-local HF exchange and the Lee–Yang–Parr (Lee et al. 1988) GGA correlation term. The equation which describes the Becke-LYP scheme is (Stephens et al, 2004):

$$E_{XC}^{BLYP} = (1-a)E_X^{LSDA} + aE_X^{HF} + bE_X^{B88} + cE_C^{LYP} + (1-c)E_C^{VWN} \quad (3.1)$$

where E_X^{HF} is the Hartree-Fock exchange term, E_X^{LSDA} is the local Spin-Density Approximation (LSDA) exchange term, E_X^{B88} is the Generalized Gradient Approximation (GGA) exchange correction due to the Becke (1988), E_C^{LYP} and E_C^{VWN} are respectively the Lee-Yang_Parr and Vosko-Wilk-Nusair LSDA correlation terms, while a, b and c are empirical parameters found to optimize the functional performance.

As for the ringwoodite and periclase phases the classical B3LYP (Becke 1993) exchange-correlation functional was employed, while for the perovskite structure, the Becke-LYP scheme with a 25% of HF exchange was adopted.

The Becke-LYP scheme is one of the most popular Hamiltonian and has been successfully applied to several cases concerning the compression of minerals.

Another effective Hamiltonian, WC1LYP (Wu and Coen, 2006), has been recently formulated and seems to provide a more accurate estimation of elastic properties and

vibrational frequencies (Demichelis et al., 2010; Prencipe et al., 2010;Ungureanu et al., 2010).

In the Wu-Cohen GGA approximation E_X^{WC} for the exchange term is adopted and the original form of Lee-Yang-Parr correlation is used:

$$E_{XC}^{WC1LYP} = 0.84E_X^{WC} + 0.16E_X^{HF} + E_C^{LYP} \quad (3.2)$$

The functional contains 16% of the exact Hartree-Fock term.

In the present work, as for the perovskite case, the WC1LYP Hamiltonian has been also applied and the obtained results have been compared with those obtained with the Becke-LYP approximation.

For all structures, the adopted choices yielded equilibrium geometry close to the experimental one measured at room temperature.

It is worth to say that, as already observed for the Pbca enstatite- Pbcn protoenstatite phase transition (Merli et al. 2011), the use of different Hamiltonians does not affect significantly the main features of the topology of the electron densities. The local functions (basis sets) to construct the crystalline orbitals were chosen as a Gaussian-type. In particular, the basis sets 8-511d1G (Valenzano 2006), 88-31G* (Nada 1996) and 8-411 (Towler 1994) have been used for Mg, Si and O, respectively. The coefficients of the outer valence functions have been reoptimized. The following default values have been used for the tolerances related to the evaluation of Coulomb and exchange series appearing in the SCF equation: 10^{-6} for coulomb overlap tolerance, 10^{-6} for coulomb penetration tolerance, 10^{-6} for exchange overlap tolerance, 10^{-6} for exchange pseudo-overlap in the direct space, and 10^{-12} for exchange pseudo overlap in the reciprocal space (Saunders et al. 2003). SCF convergence was controlled by using a threshold of 10^{-7} a.u. The default-pruned (55,434) p grid for the calculation of the integrals was chosen. The reciprocal space has been sampled according to a regular sublattice with a shrinking factor IS equal to 6 corresponding to 16

k-points in the sampling of the irreducible Brillouin zone (Dovesi et al. 2009). To address the compression mechanism, calculations have been performed at different unit cell volumes (corresponding to different pressures). The FIXINDEX option, which ensure the same set of one-electron and two-electron integrals for slightly different volumes, has been used to reduce the numerical noise when the lattice parameters is changed. The internal coordinates have been optimized at each unit cell volume by using the CVOLOPT keyword which keeps the volume constant. Convergence in the geometry optimization process has been tested on the root-mean-square (RMS) and the absolute value of the largest component of both the gradients and nuclear displacements. The thresholds for the maximum and the RMS forces (the maximum and the RMS atomic displacements) have been set to 0.00045 and 0.00030 a.u. and those for the maximum and the RMS atomic displacements to 0.00180 and 0.00120 a.u.. Geometry optimization has been terminated when all four conditions were simultaneously satisfied and restarted. The FINALRUN option has been used in order to restart the optimization, keeping the integrals classification based on the new geometry, until full stable optimization is achieved. To address the compression mechanism, calculations have been performed at different unit cell volumes and the energies obtained as function of the volumes have been fitted by means of the Birch-Murnaghan equation.

At each cell volume, the topological analysis of the calculated electron density (Bader 1994) has been performed by means of the TOPOND 98 program (Gatti 1999) and TOPOND09 (Gatti, private communication). Since TOPOND98 reads the wave function as written by CRYSTAL 98, when it has been used, wave functions have been recalculated with this previous version of the CRYSTAL program.

Chapter 4

Results and discussion:Equation of state

As already stated, in order to characterize the pressure-induced phase transitions (Ringwoodite →Mg-perovskite + periclase and Mg-perovskite → post-perovskite), the evolution of the electron arrangement in the ringwoodite and perovskite crystal structures at the different cell volumes has been investigated in terms of the topology of the electron density. The compression process has been thus simulated by performing calculations at different unit cell volumes (corresponding to different pressures). It is worth to recall that the volume was kept constant at each simulation run by using the keyword CVOLOPT.

As for the ringwoodite and periclase structures an isotropic compression of the cubic unit-cells has been reasonably assumed, and therefore only the positional coordinates of the atoms were optimized. On the contrary, in the case of the orthorhombic perovskite structure, the lattice parameters were also optimized. The results of these optimizations, obtained by applying both the Becke-LYP and the WC1LYP Hamiltonians are reported in Table 4.1.

Volume (Å^3)	a (Å)	b (Å)	c (Å)
120.06	4.2614	4.5334	6.2146
121.03	4.2763	4.5417	6.2316
122.43	4.2968	4.5550	6.2553
126.18	4.3525	4.5887	6.3177
130.06	4.4070	4.6239	6.3824
134.70	4.4696	4.6665	6.4582
139.89	4.5355	4.7134	6.5435
143.92	4.5844	4.7500	6.6092
145.92	4.6072	4.7674	6.6435
147.92	4.6295	4.7852	6.6771
149.92	4.6523	4.8030	6.7094
151.92	4.6742	4.8210	6.7417
154.92	4.7061	4.8481	6.7902
156.92	4.7269	4.8660	6.8223
159.92	4.7576	4.8929	6.8700
162.42	4.7827	4.9151	6.9093
164.57	4.8051	4.9348	6.9404

Table 4.1. Lattice parameters obtained from the optimization of the perovskite structure a the difefrent cell volumes by applying the Becke-LYP Hamiltonian

Volume (Å^3)	a (Å)	b (Å)	c (Å)
115.04	4.1811	4.4873	6.1317
116.01	4.1953	4.4971	6.1490
117.03	4.2107	4.5067	6.1671
117.97	4.2254	4.5152	6.1835
119.02	4.2415	4.5249	6.2015
120.06	4.2570	4.5345	6.2195
121.02	4.2717	4.5432	6.2361
122.43	4.2917	4.5564	6.2608
125.02	4.3294	4.5802	6.3048
128.02	4.3718	4.6073	6.3557
130.06	4.3996	4.6263	6.3898
133.98	4.4522	4.6622	6.4546
138.03	4.5045	4.6994	6.5208
141.99	4.5537	4.7355	6.5847
146.00	4.6019	4.7719	6.6483
150.01	4.6482	4.8078	6.7126
152.04	4.6707	4.8262	6.7446
155.00	4.7041	4.8527	6.7901
156.38	4.7184	4.8655	6.8119
157.99	4.7364	4.8798	6.8357
159.92	4.7560	4.8967	6.8668
162.53	4.7835	4.9194	6.9067
164.95	4.8082	4.9404	6.9440

Table 4.2. Lattice parameters obtained from the optimization of the perovskite structure a the different cell volumes by applying the WC1LYP Hamiltonian

From the data reported in Tables 4.1 and 4.2 it can be observed that the two functional give very similar results. In fact, when the Becke-Lyp functional is employed the optimization of the more compressed structures revealed unfeasible.

The anisotropy of the system is evidenced by the relative diminution of the lattice parameters on decreasing the cell volume (see Figure 4.1 and 4.2).

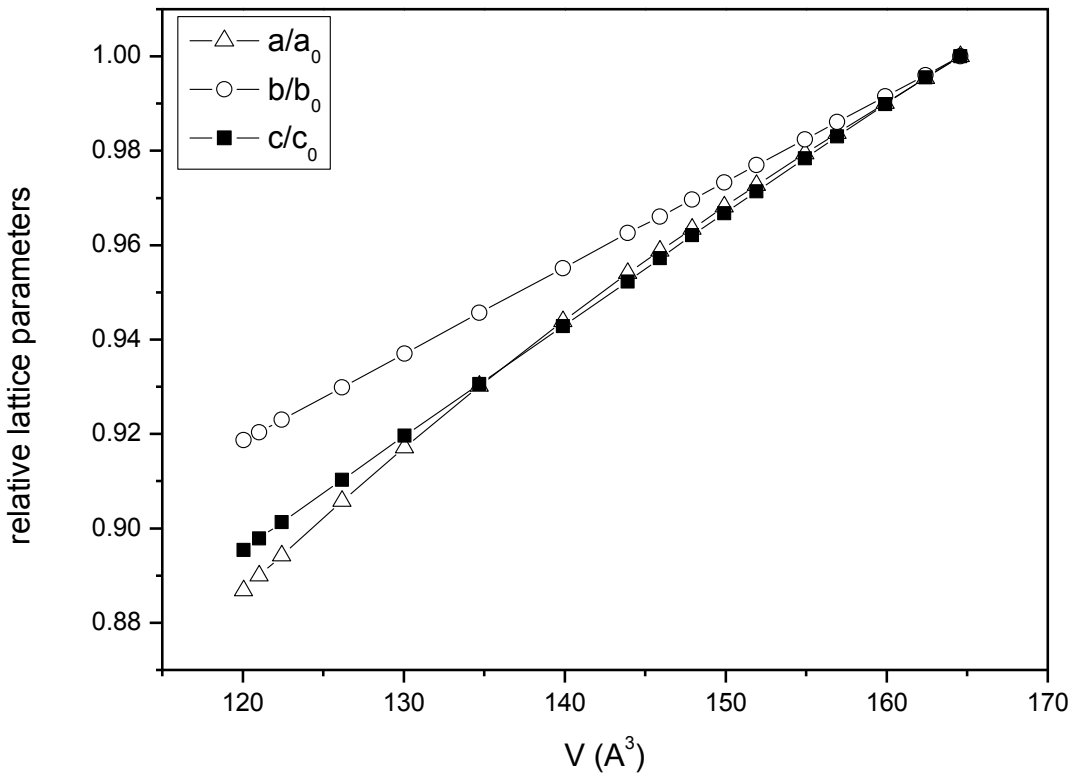

Figure 4.1 Relative lattices parameters obtained from the optimization of the perovskite structure at the different cell volumes by applying the WC1LYP Hamiltonian

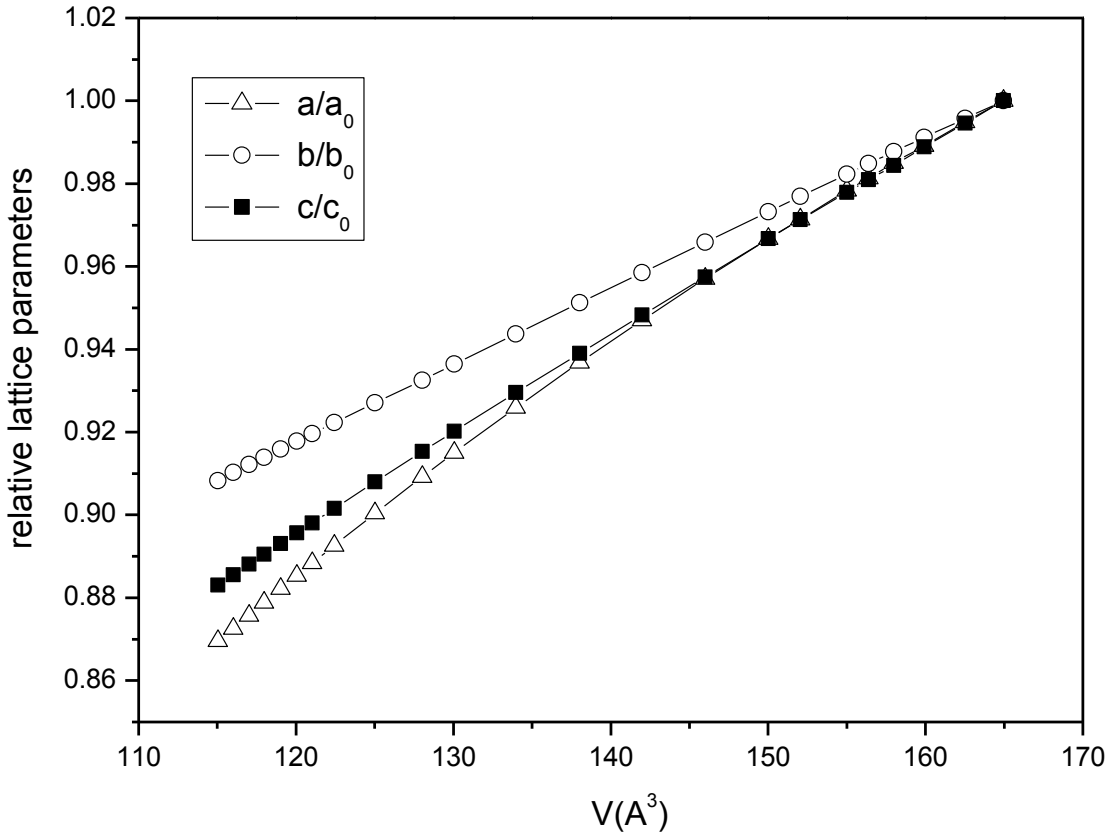

Figure 4.2 Relative lattices parameters obtained from the optimization of the perovskite structure at the different cell volumes by applying the WC1LYP Hamiltonian

Perusal of the figures indicates that the b axes is the less compressible one.

The E(V) data obtained for each of the three structures (reported in Figure 4.3) have been used to determine the correct value of pressure associated with each cell volume, by constructing the corresponding equations of state.

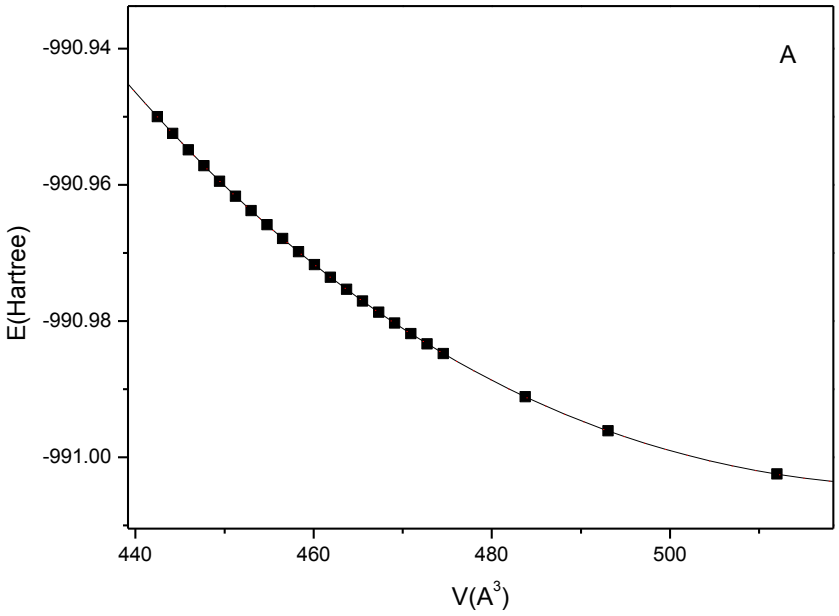
A
-990.94
-990.96
-990.98
-991.00
E(Hartree)
440
460
480
500
V(A3)

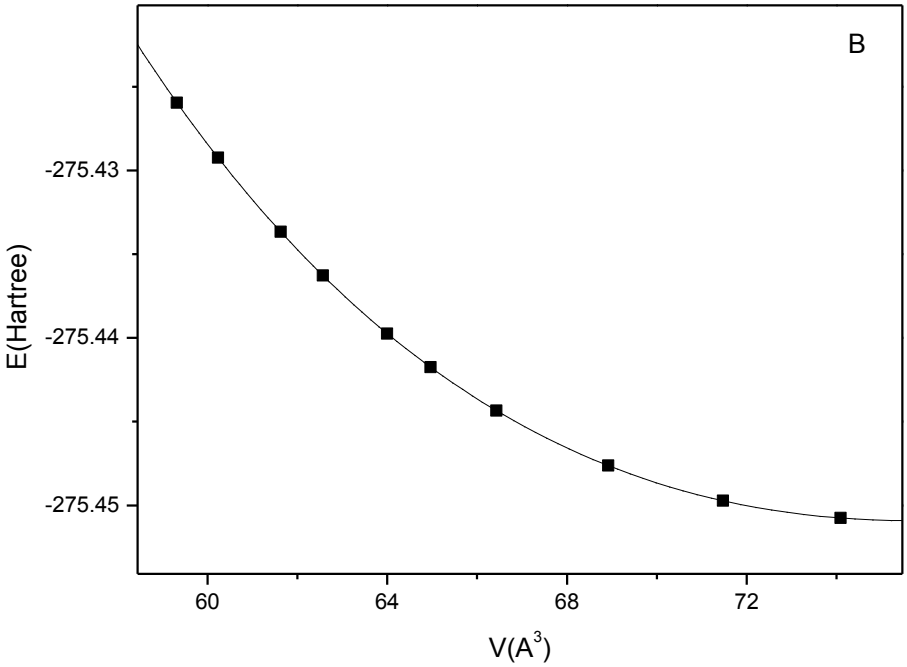
B
-275.43
-275.44
-275.45
E(Hartree)
60
64
68
72
V(A3)

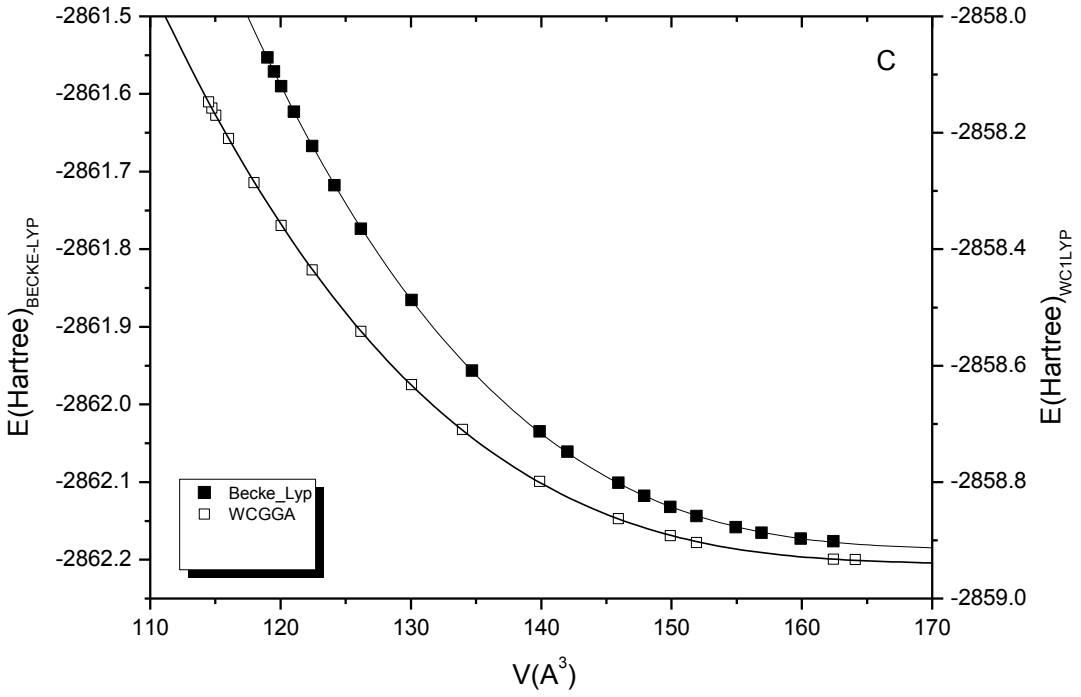

Figure 4.3. Equation of state for (A) ringwoodite, (B) periclase e (C) perovskite structures obtained from interpolation of the 3rd-order Birch-Murnhagan equation of state.

The E(V) data obtained for each of the three structures have been fitted by means of different equations of state, namely the Murnhagan , the second-order Birch-Murnhagan, the third-order Birch-Murnaghan equation, and the Vinet equation of state (see Table 4.3).

Murnhagan	$E(V) = E_0 + \frac{K_0 V}{K_0'}\left(\frac{(V_{0/} - V)^{K_0'}}{K_0' - 1}\right) - \frac{K_{0_j} V_0}{K_0' - 1}$
2nd order Birch-Murnhagan	$E(V) = E_0 - \frac{9}{8} K_0 V_0 \left[\left(\frac{V_0}{V}\right)^{\frac{2}{3}} - 1\right]^2$
3rd order Birch-Murnhagan	$E(V) = E_0 - \frac{9K_0V_0}{16}\left\{\left[\left(\frac{V_0}{V}\right)^{\frac{2}{3}} - 1\right]^3 K' + \left[\left(\frac{V_0}{V}\right)^{\frac{2}{3}} - 1\right]^2 \left[6 - 4\left(\frac{V_0}{V}\right)^{\frac{2}{3}}\right]\right\}$
3rd order Vinet	$E(V) = E_0 + \frac{4K_0V_0}{(K_0^{'} - 1)^2} - 2V_0K_0(K_0^{'} - 1)^{-2}(5 + 3K_0^{'}\left[\left(\frac{V_0}{V}\right)^{\frac{2}{3}} - 1\right] - 3\left(\frac{V_0}{V}\right)^{\frac{2}{3}})\exp(-\frac{3}{2}(K_0^{'} - 1)(\left(\frac{V_0}{V}\right)^{\frac{2}{3}} - 1))$

Table 4.3. List of the equations of state applied in the present work

The obtained values of V_0 (volume at minimum energy), K_0 (zero-pressure bulk modulus) and K' (pressure derivative of K at P=0) are reported in Table 4.4.

V_0 ($Å^3$)	K_0 (GPa)	K' ($10^{-3}GPaK^{-1}$)	References
Ringwoodite			
529.3	200.2	3.4	*This study (Murnhagan EoS, B3LYP)*
530.8	190.7	-	*This study(2nd order Birch- Murnhagan EoS ,B3LYP)*
530.1	196.4	3.8	*This study (3rd order Birch- Murnhagan EoS, B3LYP)*
530.2	195.0	3.9	*This study (Vinet EoS, B3LYP)*
530.9	196.4	4.3	*Ottonello et al. (2009)(calculated, static)*
531.7	193.3	4.3	*Ottonello et al. (2009) (calculated, 298.15 K)*
539.1	176.0	-	*Piekarz et al. (2002) (calculated, static)*
527.5	184.6	4.5	*Yu and Wentzcovitch (2006) (calculated, 300K)*
523.9	190.3	4.1	*(Kiefer et a., 1999) (experimental, extrapolated at zero temperature)*
526.7	182.0	4.2	*Meng et al. (1994) (experimental, 300K)*
524.8	182	4.6	*Katsura et al. (2004) (experimental, 300K)*
-	185	-	*Jackson et al. (2000) (experimental, 300K)*
Mg-Perovskite			
164.6	265.7	3.4	*This study (Murnhagan EoS, WC1LYP)*
165.2	247.6	-	*This study(2nd order Birch- Murnhagan EoS, WC1LYP)*
164.9	254.5	3.9	*This study (3rd order Birch- Murnhagan EoS, WC1LYP)*
165.0	248.9	4.2	*This study (Vinet EoS, WC1LYP)*
164.5	262.9	3.4	*This study (Murnhagan EoS, Becke-LYP)*
165.0	247.8	-	*This study (2nd order Birch- Murnhagan EoS, Becke-LYP)*
164.8	252.5	3.9	*This study (3rd order Birch- Murnhagan EoS, Becke-LYP)*
164.7	255.4	3.8	*This study (4th order Birch-Murnhagan EoS, Becke-LYP)*
164.9	247.2	4.2	*This study (Vinet EoS, Becke-LYP)*
165.0	240.6	4.6	*This study (3rd order Natural Strain EoS, Becke-LYP)*
164.7	255.1	3.8	*This study (4th order Natural Strain EoS, Becke-LYP)*
162.4	267	4.1	*Oganov et al. (2001), (calculated, static)*
162.5	257	4.0	*Karki et al. (1997), (calculated, static)*
163.35	259.82	4.06	*Oganov et al. (2004) (calculated, static, LDA)*
167.42	230.05	4.14	*Oganov et al. (2004) (calculated, static, GGA)*
162.5	264.0	3.8	*Li-Wei et al. (2006)(experimental, extrapolated at zero temperature)*
162.5	264.0	-	*Yeganeh-Haeri et a.l (1994) (experimental, 300K)*
162.3	261.0	4.0	*Shim et al. (2000) (experimental, 300K) , Funamori et al.(1996)*
162.3	259.5	3.69	*Oganov et al. (2004) (experimental, 300K))*
162.40	250	-	*Sinogeikin et. al (2004) (experimental, 300K)*
162.39	256	3.8	*Katsura et al. (2009) (experimental, 300K)*
Periclase			
75.6	168.2	3.7	*This study (Murnhagan EoS, B3LYP)*
75.6	166.7	-	*This study(2nd order Murnhagan EoS, B3LYP)*
75.6	163.8	4.1	*This study (3rd order Murnhagan EoS, B3LYP)*
75.7	161.3	4.3	*This study (Vinet EoS, B3LYP)*
76.59	150.8	4.0	*Oganov et al. (2003)(calculated, static)*
74.6	160	4.0	*Li-Wei et al. (2006)(experimental, extrapolated at zero*

74.7	159.9	4.1	*Dewaele et al. (2000)(experimental, 298K)*
74.71	160.9	4.3	*Kono et al. (2010) (experimental, 300K)*

Table 4.4. Equation of State parameters (volume at minimum energy, V_0, zero-pressure bulk modulus K_0 and pressure derivative of K at P=0, K') of ringwoodite, periclase and Mg-perovskite obtained in the present study compared with previous theory and experimental studies.

The fitting parameters reported in Table 4.4 are in good accordance with those obtained from previous computational and experimental studies.

The pressure values corresponding to each volume have been determined by introducing the fitting parameters in the corresponding P(V) equations (Table 4.5).

Murnhagan	$P(V) = \frac{K_0}{K_0'}\left[\left(\frac{V}{V_0}\right)^{-K_0'} - 1\right]$
2nd order Birch-Murnhagan	$P(V) = \frac{3}{2}K_0\left[\left(\frac{V}{V_0}\right)^{-\frac{7}{3}} - \left(\frac{V}{V_0}\right)^{-\frac{5}{3}}\right]$
3rd order Birch-Murnhagan	$P(V) = \frac{3}{2}K_0\left[\left(\frac{V}{V_0}\right)^{-\frac{7}{3}} - \left(\frac{V}{V_0}\right)^{-\frac{5}{3}}\right]\left\{1 + \frac{3}{4}(K' - 4)\left[\left(\frac{V}{V_0}\right)^{-\frac{2}{3}} - 1\right]\right\}$
3rd order Vinet	$P(V) = 3K_0\left[1 - \left(\frac{V}{V_0}\right)^{\frac{1}{3}}\right]\left(\frac{V}{V_0}\right)^{-\frac{2}{3}} \exp\left\{\frac{3}{2}(K' - 1)\left[1 - \left(\frac{V}{V_0}\right)^{\frac{1}{3}}\right]\right\}$

Table 4.5. List of the P(V) equations of state applied in the present work

In the following figure the equations of state for the three investigated structures are reported. For the sake of clarity only the curve fitting obtained from the application of the 3rd order Birch-Murnhagan equation is showed.

Note that, since it is well known that the perovskite phase is stable at the very high pressure values typical of the Earth's lower mantle, for this mineralogical phase the pressure range investigated is wider than in the other two cases.

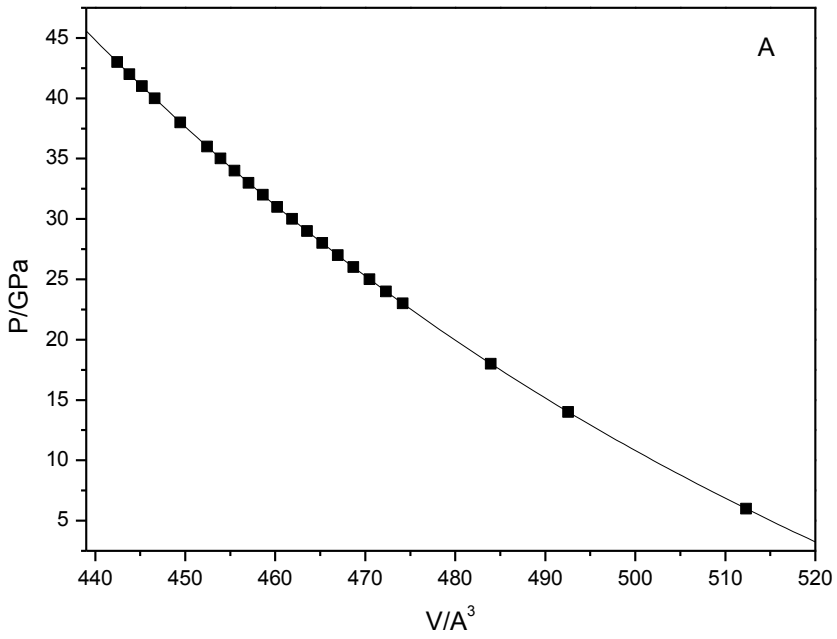

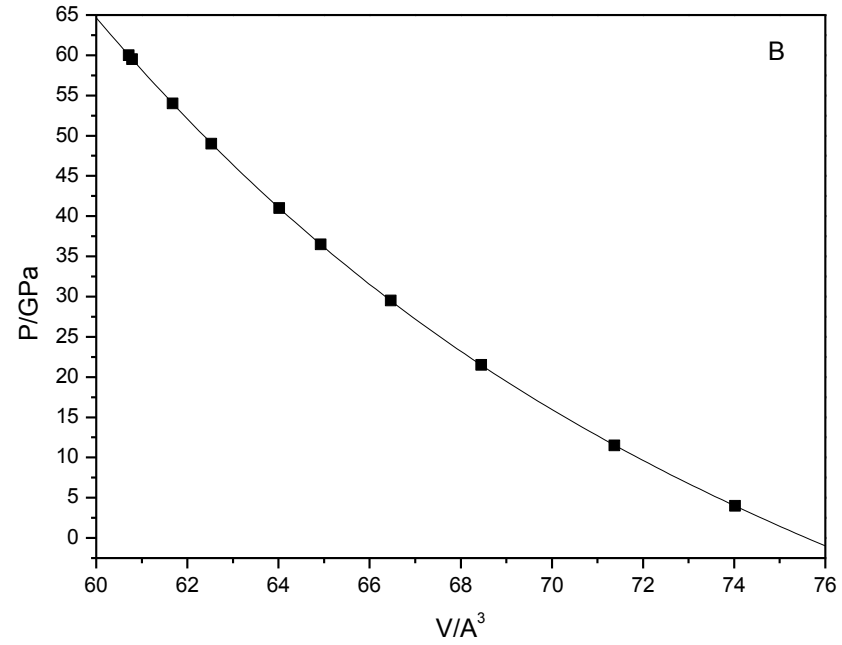

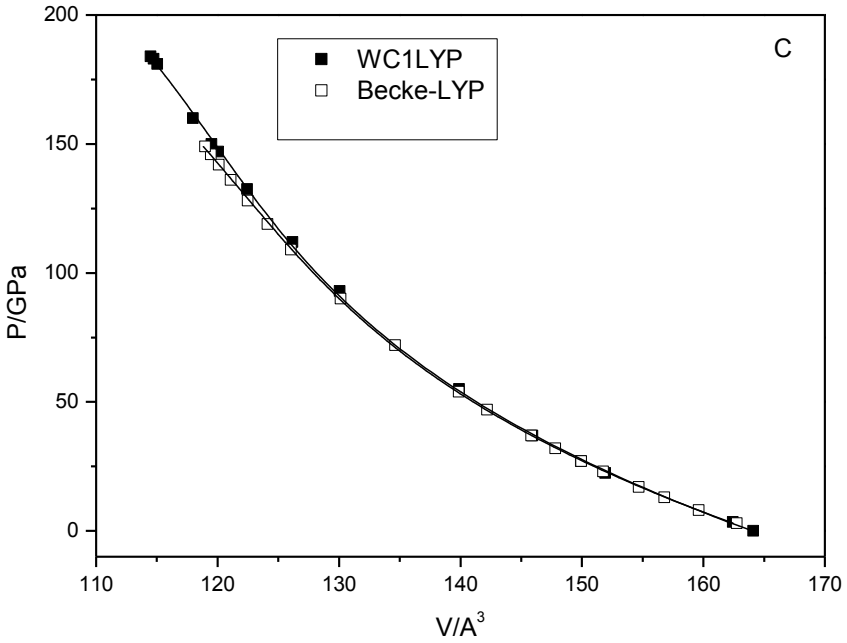

Figure 4.4. Equations of states for (A) ringwoodite, (B) periclase and (C) Mg-perovskite obtained from interpolation of the 3-order Birch-Murnnaghan equation of state.

Perusal of figure 4.4 indicates that the relationship obtained applying the two functional is very similar even though the WC1LYP functional allows us to span an higher pressure range (up to 182 GPa) than the Becke-LYP (up to 150 GPa). The construction of the equations of state allowed us not only to identify the pressure value where the Cps is observed to change, but also to determine the most stable structure on the basis of the computed enthalpies (H).

In a second step, aiming at obtaining the volume, energy and enthalpy values corresponding to the same pressure values for all the three investigated phases, the following procedure has been applied:

1. Eq. 2 has been numerically solved and the volumes corresponding to the desired pressure values have been determined in the range 0-100 GPa.
2. The obtained volumes have been introduced in Eq.1 in order to determine the energy values corresponding to the desired pressure values.
3. The product PV has been added to the calculated energy in order to determine the enthalpy values, which have been used to determine the most stable structure at finite pressure and T = 0 K.

Figure 4.5 shows the theoretical enthalpies of the ringwoodite phase and that of the sum of MgO and Mg-perovskite plotted against pressure.

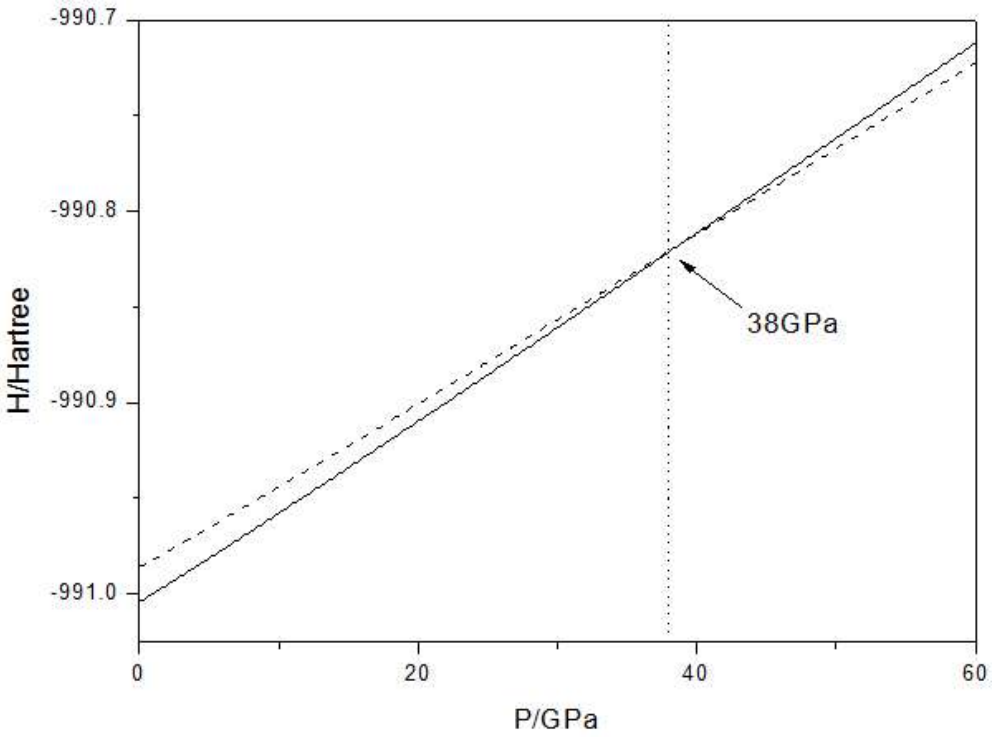

Figure 4.5. Calculated enthalpies per formula unit of ringwoodite (solid line) and of the assembly MgO + MgSiO3 (dashed line) versus pressure

Perusal of the figure clearly indicates that the energy differences involved in the reaction are quite small and that, at zero-temperature, ringwoodite phase transforms in Mg-perovskite and MgO at ~38 GPa. As already mentioned, the phase boundary pressure between ringwoodite and perovskite was found to be ~21-24 GPa at 1550-2100 K (Chudinovskikh & Boehler 2001, Katsura et.al. 2003, Shim et al. 2001). The higher value of pressure transition obtained from our calculation can be explained in the light of a negative Clapeyron slope (Katsura et.al. 2003; Deuss 2006; Fei et al. 2004), which implies an increase of the transition pressure on decreasing the temperature. Moreover it has to be noted that, as already mentioned, the PT point obtained from the present study refers to the completely anhydrous and totally ordered pure γ-Mg_2SiO_4, Mg-perovskite and periclase,

while the experimentally determined PT points at higher temperature refers to samples where water, impurities or structural disorder also contribute to the localization of the phase boundary by promoting the phase transitions and decreasing the transition pressure (Katsura et.al. 2003).

Chapter 5

Result and discussion: Topological analysis of the ringwoodite electron density

The Bader topological analysis applied to the electron density of the ringwoodite, for pressure values ranging from 0 to ~33 GPa, revealed the presence of 8 different critical points, while, at higher pressure values, the appearance of two more critical points, namely a bond and a ring critical point, has been observed.

It is worth to say that the Eulero's rule (Bader 1992) is satisfied in the whole pressure range investigated.

The complete list of CPs are reported in Table 5.1 for two different cell volumes (corresponding to pressures of 7.3 GPa and 45.7 GPa) while in Fig.5.1 and Fig.5.2 the ringwoodite structures with the related bond and ring critical points are depicted. Note the presence of two more critical point (BCP4 and RCP4) in the structure corresponding to the higher pressure (Fig.5.2).

	P=7.3 GPa					P=45.7GPa				
CP's	x(au)	y(au)	z(au)	ρ(au)	$\nabla^2\rho$(au)	x(au)	y(au)	z(au)	ρ(au)	$\nabla^2\rho$(au)
BCP1	0.175	0.175	0.175	0.137	0.615	0.175	0.175	0.175	0.154	0.817
BCP2	0.248	0.248	0.389	0.043	0.280	0.249	0.249	0.389	0.055	0.394
BCP3	0.375	0.245	0.375	0.016	0.051	0.375	0.247	0.375	0.021	0.071
RCP1	0.079	0.175	0.334	0.011	0.043	0.076	0.175	0.333	0.014	0.057
RCP3	0.363	0.245	0.387	0.016	0.052	0.358	0.247	0.391	0.021	0.076
CCP1	0.000	0.000	0.000	0.006	0.026	0.000	0.000	0.000	0.008	0.033
CCP2	0.375	0.375	0.375	0.007	0.029	0.375	0.375	0.375	0.010	0.041
CCP3	0.125	0.125	0.378	0.009	0.036	0.125	0.125	0.377	0.011	0.048
BCP4	-	-	-	-	-	0.250	0.138	0.388	0.022	0.082
RCP4	-	-	-	-	-	0.250	0.141	0.391	0.022	0.084

Table 5.1. Fractional Coordinates (x, y, z) , electron density (ρ) and Laplacian of the electron density ($\nabla^2\rho$) of the critical points for the ringwoodite structure corresponding to two different pressure values.

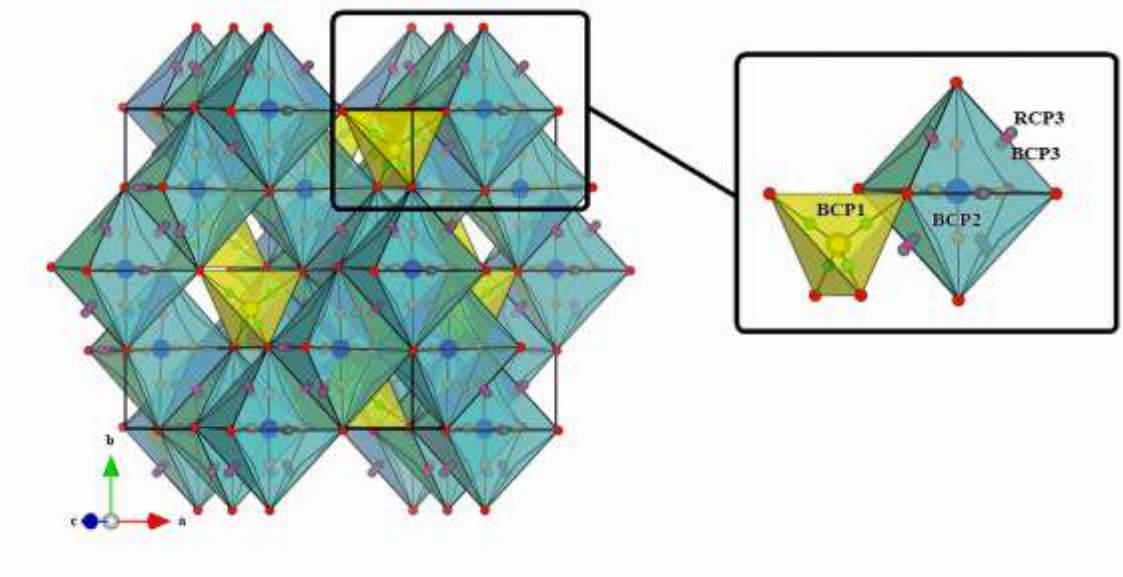

Figure 5.1 Projection onto the (201) plane of the structure of ringwoodite at P=7.3 GPa with the related bond and ring critical points. The inset is the enlargement of the selected rectangle.

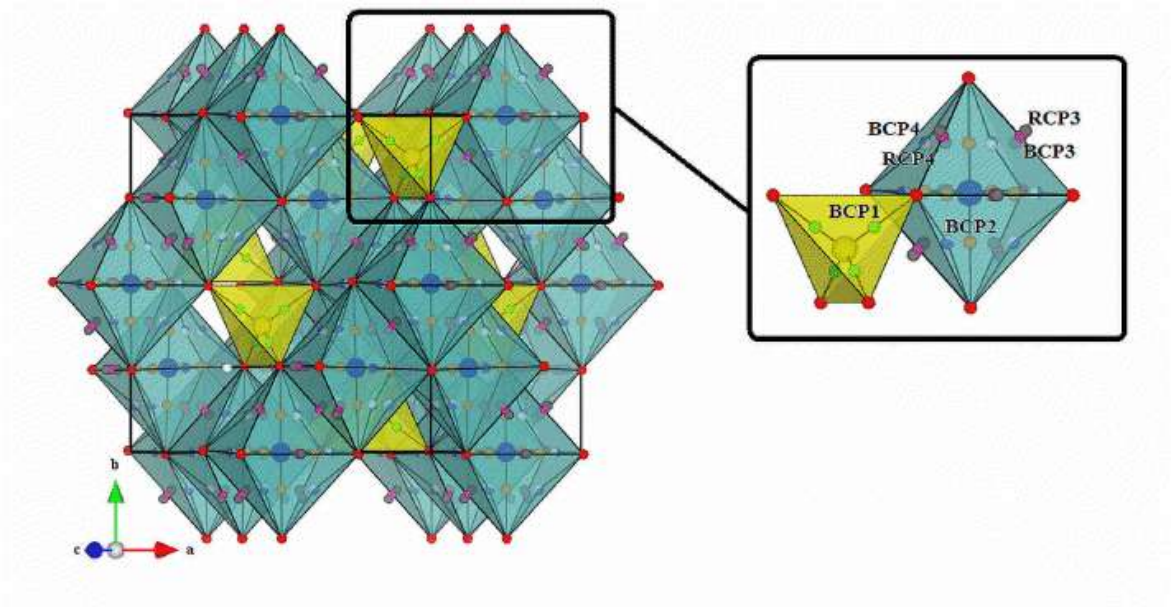

Figure 5.2 Projection onto the (201) plane of the structure of ringwoodite at P=45.7 GPa with the related bond and ring critical points. The inset is the enlargement of the selected rectangle.

In order to obtain more information about the chemical bonds, some topological properties related to the BCPs, namely the electron density, $\rho(\mathbf{r})$, the Laplacian of the electron density, $\nabla^2\rho(\mathbf{r})$, the eigenvalues λ_i's and the ellipticity ε (defined $\varepsilon = |\lambda_1|/|\lambda_2|-1$) have been investigated. In Table 3 these data are reported for eight different values of pressure.

The trends of the topological variables as a function of the pressure are consistent with those observed by Prencipe & Nestola (2007) in the case of the beryl: as the atomic distances decrease due to the pressure load, the electron density $\rho(\mathbf{r})$, the Laplacian of the electron density, $\nabla^2\rho(\mathbf{r})$, and the $|\lambda_i|$ values increase. It has been proposed (Prencipe & Nestola 2007) that the increase of $\rho(\mathbf{r})$ with the pressure is a consequence of the BCP getting closer to the nucleus, where $\rho(\mathbf{r})$ has a maximum, as the bond distance is reduced.

	ρ	$\nabla^2\rho$	λ_1	λ_2	λ_3	ε
P/Gpa			**BCP1 (Si-O)**			
0.2	0.135	0.593	-0.248	-0.248	1.091	0.00
7.3	0.137	0.615	-0.254	-0.254	1.123	0.00
16.3	0.141	0.664	-0.266	-0.266	1.197	0.00
27.9	0.146	0.726	-0.281	-0.281	1.29	0.00
32.6	0.149	0.751	-0.288	-0.288	1.327	0.00
35	0.15	0.771	-0.293	-0.293	1.356	0.00
45.7	0.154	0.817	-0.304	-0.304	1.425	0.00
50.1	0.156	0.838	-0.309	-0.309	1.460	0.00
			BCP2 (Mg-O)			
0.2	0.041	0.266	-0.060	-0.059	0.385	0.01
7.3	0.043	0.28	-0.063	-0.062	0.405	0.01
16.3	0.046	0.309	-0.069	-0.068	0.446	0.01
27.9	0.05	0.344	-0.077	-0.076	0.497	0.01
32.6	0.051	0.358	-0.080	-0.079	0.516	0.01
35	0.052	0.368	-0.082	-0.081	0.531	0.01
45.7	0.055	0.394	-0.088	-0.087	0.568	0.01
50.1	0.056	0.405	-0.090	-0.089	0.585	0.01
			BCP3 (O-O)			
0.2	0.0160	0.0480	-0.0121	-0.0008	0.0612	14.8
7.3	0.0163	0.0510	-0.0125	-0.0010	0.0645	11.3
16.3	0.0176	0.0560	-0.0137	-0.0016	0.0716	7.4
27.9	0.0191	0.0624	-0.0152	-0.0025	0.0801	5.2
32.6	0.0197	0.0648	-0.0158	-0.0027	0.0834	4.8
35	0.0202	0.0669	-0.0163	-0.0029	0.0859	4.5
45.7	0.0213	0.0714	-0.0175	-0.0034	0.0923	4.1
50.1	0.0217	0.0735	-0.0179	-0.0037	0.0951	3.9
			BCP4(O-O)			
35	0.0215	0.0788	-0.0180	-0.0010	0.0979	17.1
45.7	0.0222	0.0821	-0.0187	-0.0019	0.1027	8.8
50.1	0.0263	0.0842	-0.0192	-0.0022	0.1056	7.7

Table 5.2. Electron density (ρ), Laplacian of the electron density ($\nabla^2\rho$), eigenvalues (λi's) and ellipticity (ε) for each typology of atom-atom interaction at given pressure values in the range 0-50 GPa.

Moreover, the parallel increase of the negative ($\lambda_{1,2}$) and positive (λ_3) curvatures of $\rho(\mathbf{r})$ in the planes normal to the bond axes and in the directions normal to them could be due to the

increase of the potential scalar field along the bond regions, as bond distances are reduced. In other words, on increasing the positive potential as nuclei get closer to one another the electrons are attracted in the interatomic region and, at the same time, they are removed from the region about the critical point, and shifted toward each nucleus, due to the requirement imposed by the antisymmetry principle on the electronic wave function (Bader 1994). As expected, the value of the ellipticity is very large in the case of the weak O-O interactions.

	Magnesium				Silicon				Oxygen			
GPa	**N(Ω)**	**q(Ω)**	**V(Ω)**	**I(Ω)**	**N(Ω)**	**q(Ω)**	**V(Ω)**	**I(Ω)**	**N(Ω)**	**q(Ω)**	**V(Ω)**	**I(Ω)**
0.2	10.26	1.74	28.23	1.23	10.84	3.16	23.32	0.81	9.66	-1.66	89.26	2.89
7.3	10.26	1.74	27.28	1.23	10.82	3.18	22.05	0.80	9.67	-1.67	84.30	2.87
16.3	10.26	1.74	26.37	1.22	10.80	3.20	21.10	0.79	9.67	-1.67	81.10	2.86
27.9	10.26	1.74	26.11	1.22	10.79	3.21	20.33	0.78	9.67	-1.67	77.97	2.84
32.6	10.26	1.74	25.94	1.22	10.78	3.22	20.09	0.77	9.67	-1.67	77.05	2.84
35.0	10.27	1.73	25.51	1.22	10.78	3.22	19.92	0.77	9.67	-1.67	76.44	2.84
45.7	10.27	1.73	24.66	1.22	10.77	3.24	19.51	0.76	9.67	-1.67	74.92	2.83
50.1	10.27	1.73	23.82	1.21	10.76	3.24	18.72	0.75	9.67	-1.67	71.93	2.81

Table 5.3. Atomic properties (atomic population, N(Ω), net charge, q(Ω), total atomic volume, V(Ω) and Shannon entropy I(Ω)) averaged over the basins (Ω) of Magnesium, Silicon and Oxygen atoms in the ringwoodite structure. All quantities are in a.u.

Table 5.3 lists some atomic quantities averaged over the basins (Ω) of the atoms, i.e. the atomic population, N(Ω), the net charge, q(Ω), the total atomic volume, V(Ω) and the Shannon entropy I(Ω) (defined as $I(\Omega) = -\int \rho(\mathbf{r}) \ln \rho(\mathbf{r})\, d\mathbf{r}$) in the ringwoodite structure.

It can be observed that the N(Ω), q(Ω) and I(Ω) values do not show a significant change with pressure, which can be attributed to the scarce influence of the pressure to the character of the bonds. It has to be recall that the Shannon entropy provides important information about the localization of the distribution of the electronic charge density. The

smaller value of the entropy of the electronic charge distribution for the Si atomic basin indicates a more localized charge density around this atom with respect to the Mg atomic basin. Obviously, the higher I(Ω) value for the oxygen shows that this atom has a much more delocalized electronic charge distribution due to necessity to bind, at one time, both cations and other oxygens. As for the V(Ω) values, it can be observed that the decrease of them is more significant for the O than for the Mg and Si atoms.

The evolution of the electron density across the phase transition has been further characterized by evaluating the "radial atomic expectation" value, GR(0), over the ionic basins (Ω) of Mg, Si and O atoms of the ringwoodite structure, as follows:

$$GR(0)=\int \mathbf{r}_{\omega} \bullet \nabla \rho(\mathbf{r})\, d\tau$$

where $\mathbf{r}_{\omega}$ is the radial distance of the electron from the nucleus.

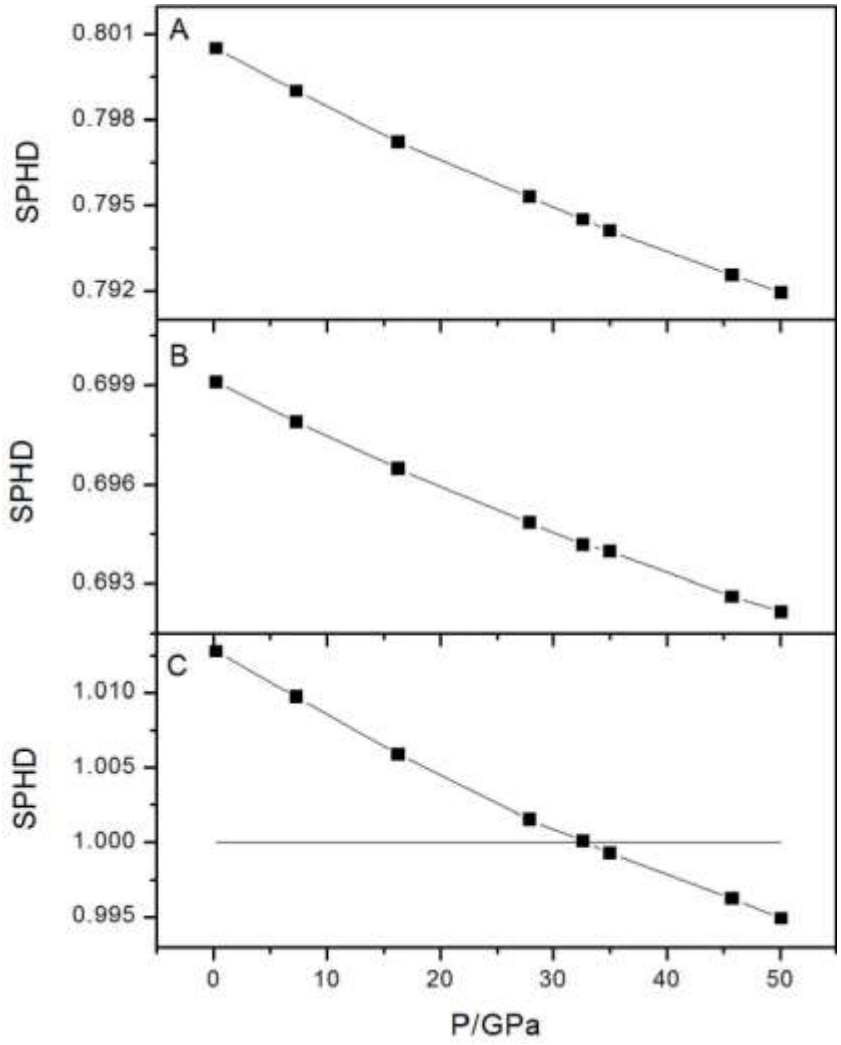

Figure 5.3. SPHD ratio as a function of the pressure for the Mg (A), Si, (B) and O (C) atoms.

The quantity GR(0) reflects the distortion of the $\nabla\rho(\mathbf{r})$ field of the charge density that is caused by the formation of chemical bond. It is worth to highlight (Bader 1994) that in the case of a free atom where the vector $\nabla\rho(\mathbf{r})$ and the radial vector $\mathbf{r}$ are parallel and oppositely directed the integral reaches its negative maximum value $-3N(\Omega)$, where $3N(\Omega)$ is the basin electron population. In a bound atom, the formation of chemical bonds distorts $\nabla\rho(\mathbf{r})$ and leads to a smaller overlap of $\mathbf{r}$ and $\nabla\rho(\mathbf{r})$.

In Fig.5 the ratio SPHD= GR(0)/[-3N], is reported as a function of the pressure for the three atoms. This ratio tends to the value of one for radial $\rho(\mathbf{r})$ and in the limit of an very weak interaction with the surroundings. Perusal of the figure indicates that, both Mg and Si atoms have their gradient vector fields $\nabla\rho(\mathbf{r})$ appreciably distorted from those of isolated atom, as indicated by the departure of SPHD from the value of unity, in the whole pressure range. On the contrary, for the O atom, at P=32.9 GPa, which is very close to the transition pressure, the SPHD value attain the value of unity, which is indicative of an extremely loosely bound atom, and therefore to a certain tendency of the atom to break the bonds with the neighboring atoms.

This result is an important topological evidence of the approaching of the phase transition and can also be taken, together with the trend of the V(Ω), as an indication of the central role played form the oxygen atoms in the pressure induced phase transition.

At this point it is challenging to interpret the topological results in the light of the catastrophe theory. As already stated, two mechanism of structural instability are predicted as a corollary of the theorem of structural stability: the *bifurcation* and the *conflict catastrophe*. Concerning this task, Merli et al.(2011) found a bifurcation type catastrophe (Fold Catastrophe) for the temperature induced enstatite-protoenstatite phase transition.

In the present case, the topological analysis performed across the pressure transition, also reveals the occurrence of a *fold catastrophe*, i.e. the appearance of two coalescent CPs (BCP4 and RCP4) corresponding to the formation of new O-O bond. At the same time a *conflict-type catastrophe* occurs since the stable and the unstable manifolds of a couple of two neighboring critical points (BCP3 and BCP4) do not intersect transversally (see Table 5).

CPs	Angles(°)							
	0.2 GPa	7.3 Gpa	16.3 Gpa	27.9 GPa	32.6 Gpa	35.0 GPa	45.7 Gpa	50.1Gpa
BCP1-BCP3	65.3	65.3	45.0	45.0	65.3	65.3	44.2	44.2
BCP1-RCP3	95.0	95.0	82.6	82.5	85.1	85.1	82.5	82.5
BCP3-RCP3	90.0	90.0	89.2	89.1	90.0	90.0	90.0	90.0
BCP2-BCP3	45.0	45.0	45.0	45.0	45.0	45.0	45.0	45.0
BCP2-RCP3	45.1	45.1	45.1	45.0	45.0	45.0	45.0	45.0
BCP1-BCP4	X	X	X	X	X	5.51	6.5	6.5
BCP1-RCP4	X	X	X	X	X	65.4	44.4	44.4
BCP4-RCP4	X	X	X	X	X	90.0	90.0	90.0
BCP2-BCP4	X	X	X	X	X	45.0	45.0	45.0
BCP2-RCP4	X	X	X	X	X	89.5	89.5	89.5
BCP3-BCP4	X	X	X	X	X	**0.0**	**0.0**	**0.0**
BCP3-RCP4	X	X	X	X	X	89.4	90.0	89.5
RCP3-BCP4	X	X	X	X	X	1.4	1.4	1.3
RCP3-RCP4	X	X	X	X	X	1.4	1.4	1.3

Table 1.3. Angles between the stable and the unstable manifolds of all the neighbouring RCPs and BCPs, at given pressure values in the range 0-50 GPa

Perusal of the data reported in Table 5.3 indicates that, for pressures values less than 33 GPa, the manifolds of all the investigated pairs intersect almost transversally, which is indicative of a stable configuration. A different situation can be observed for higher pressure values. In particular we can observe a non-transversal interaction between the bond path (unstable manifolds) of a (3,-1) critical point, namely the BCP4, with the interatomic surface (stable manifolds) of a second (3,-1) critical point, namely the BCP3. According to the *Palis-Smale's* theorem (Palis & Smale 1970) this arrangement is unstable and corresponds to a *conflict* structure.

In the light of the different nature of the two recognized catastrophe mechanisms, it is possible to establish which one is responsible for the breakdown of the ringwoodite structure. In fact, since the fold catastrophe simply corresponds to the formation of a bond,

while the conflict catastrophe give rise to the formation of an instable structure, the catastrophe mechanism to be invoked in the investigated phase transition is the conflict-type.

Further indication of the instability of the ringwoodite structure, close to the transition pressure, is the very low intersection angles between the stable and the unstable manifolds of the pairs RCP3-BCP4 and RCP3-RCP4. It is worth to say that all the involved critical points are relative to the O-O interaction, which could be taken as a further indication of the important role played form the oxygen atoms in the pressure induced phase transition.

Finally it can also be observed that the angle between the unstable manifold of the (3,-1) critical point relative to the Si-O bond (BCP1) and the stable manifold of the BCP4 is also quite low ($\alpha \approx 5°$) which can be interpreted as an indication of the weakening of the involved bonds.

The results presented in Chapters 4-5 have been published in the Journal Physics and Chemistry of Minerals (Parisi F, Sciascia L, Princivalle F, Merli M (2012). *The pressure induced Ringwoodite to Mg-perovskite and Mg-wüstite post spinel phase transition: a Bader's topologycal analysis of the ab-initio electron densities.* Physics and Chemistry of Minerals, 339, 103-113)

Chapter 6

Topological analysis of the Mg-perovskite electron density

In order to verify the reliability of this approach we performed the topological analysis of the Mg-perovskite.

First of all, the quantity GR(0), that reflects the distortion of the $\nabla\rho(\mathbf{r})$ field of the charge density caused by the formation of a chemical bond, has been investigated. It is worth to say that in the case of the Mg-perovskite both Oxygens are far away from the interesting value reached at high pressures by the ringwoodite phase. In this case the values indicate that the distortion of the $\nabla\rho(\mathbf{r})$ field enhance with pressure. No destabilization of this phase could be detected by this parameter.

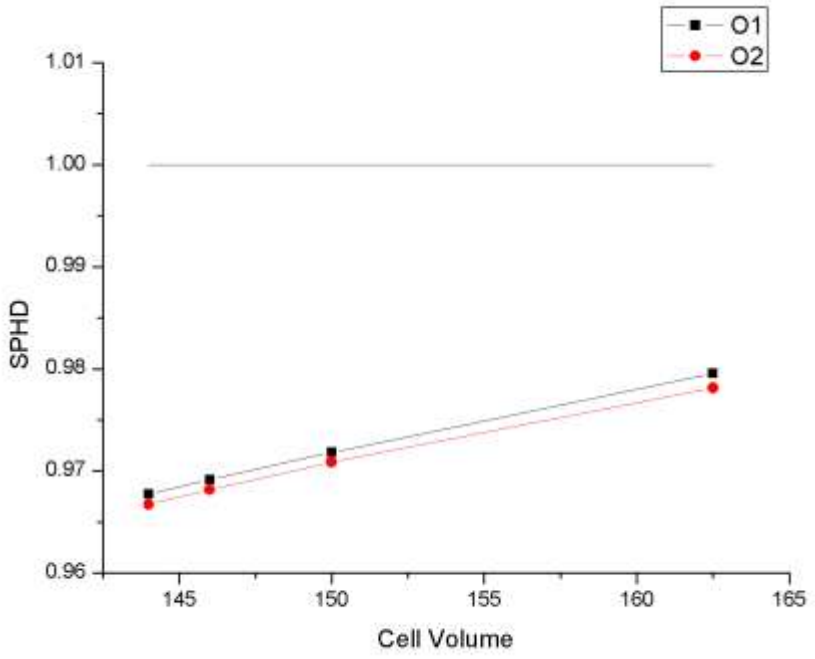

Figure 2. SPHD ratio as a function of the Mg-perovskite cell volume for Oxygen 1 and Oxygen 2

The topological analysis of the electron densities produced by both the Becke-LYP and the WC1LYP schemes provided quite similar results, and, analogously to the ringwoodite case, the Eulero's rule (Bader 1992) is always satisfied.

The study of the evolution of the topological critical points across the whole pressure range revealed very interesting features. The setting of critical points present in the structures from 0 to 140 GPa are reported in Figures 6.2 – 6.11, where, for the sake of clarity, two different planes of the crystallographic cell, namely the (001) and the (010), are presented for each investigated pressure values.

Note that, for brevity reasons, all the figures refers to the topological analysis performed on the electron density constructed by means of the WC1LYP Hamiltonian.

At low pressure values (Figure 6.2-6.3) 28 different critical points can be recognized. The most prominent features are depicted in the enlargements. In particular, Figure 6.2.b shows a region of the crystallographic cell where, at low pressure regime, no critical points are present (this figure will be compared in the following paragraph with figure 6.4.b) while in Figure 6.3.b the presence of a couple of coalescent critical points, namely a BCP along the bond path joining two oxygen atoms and a RCP (indicated as BCP1 and RCP1) and , surrounding them, two couples of critical points very close to each other, namely a cage and a ring critical points (indicated as CCP2 and RCP2) are marked.

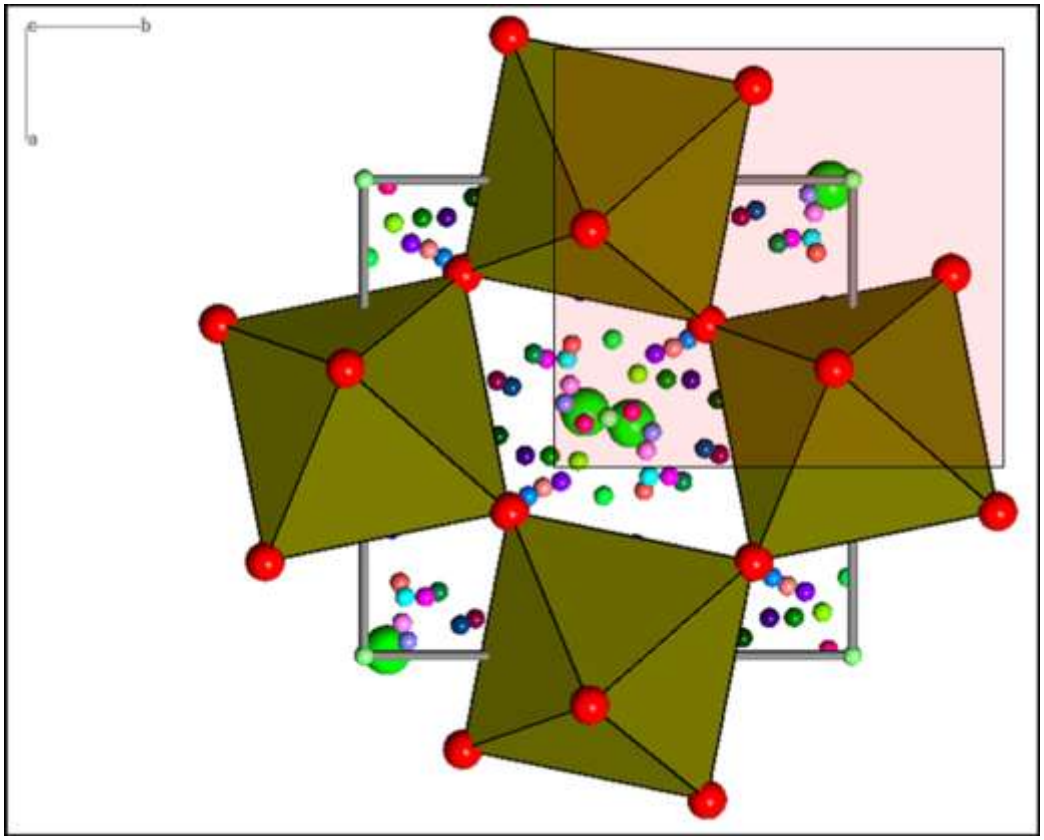

Fig.6.2.a Projection onto the (001) plane of the structure of Mg-perovskite at P = 0.0001 GPa with the related bond, ring and cage critical points. The selected rectangle is enlarged in figure 6.2.a.

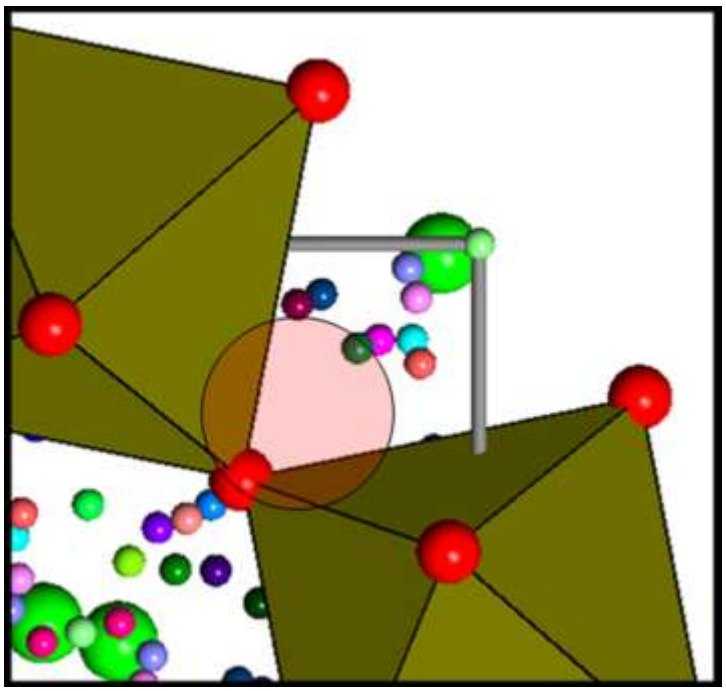

Figure 6.2.b. Enlargement of the rectangle selected in the figure 6.2.a

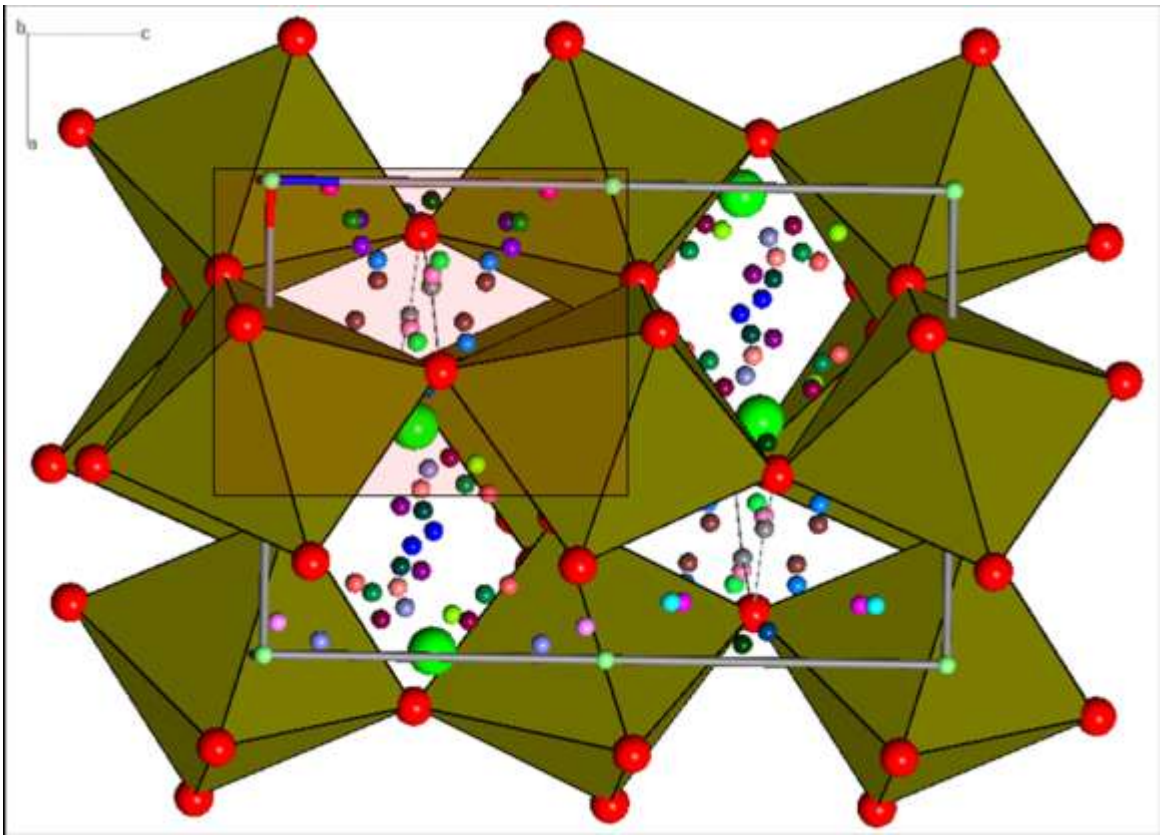

Fig. 6.3.a. Perspective view onto the $(0\bar{1}0)$ plane of the structure of Mg-perovskite at P = 0.0001 GPa
with the related bond, ring and cage critical points. The selected rectangle is enlarged in figure 6.3.b.

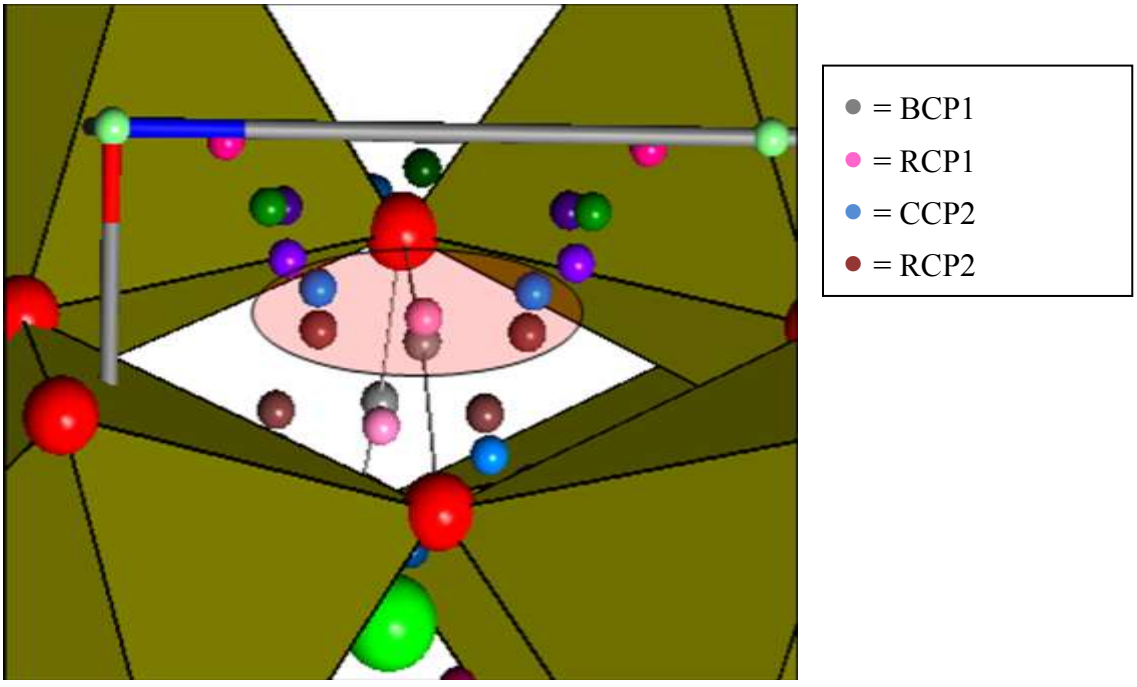

Figure 6.3.b. Enlargement of the rectangle selected in the figure 6.3.a.

The analysis of the critical points at higher pressures (Figure 6.4-6.5) revealed the appearance of a third couple of coalescent critical points, namely a cage , CCP3, and a ring, RCP3 (see Figure 6.4.b) and the simultaneous decrease of the distance CCP2-RCP2, while the distance BCP1-RCP1 is not affected from the pressure increase (Figure 6.5.b).

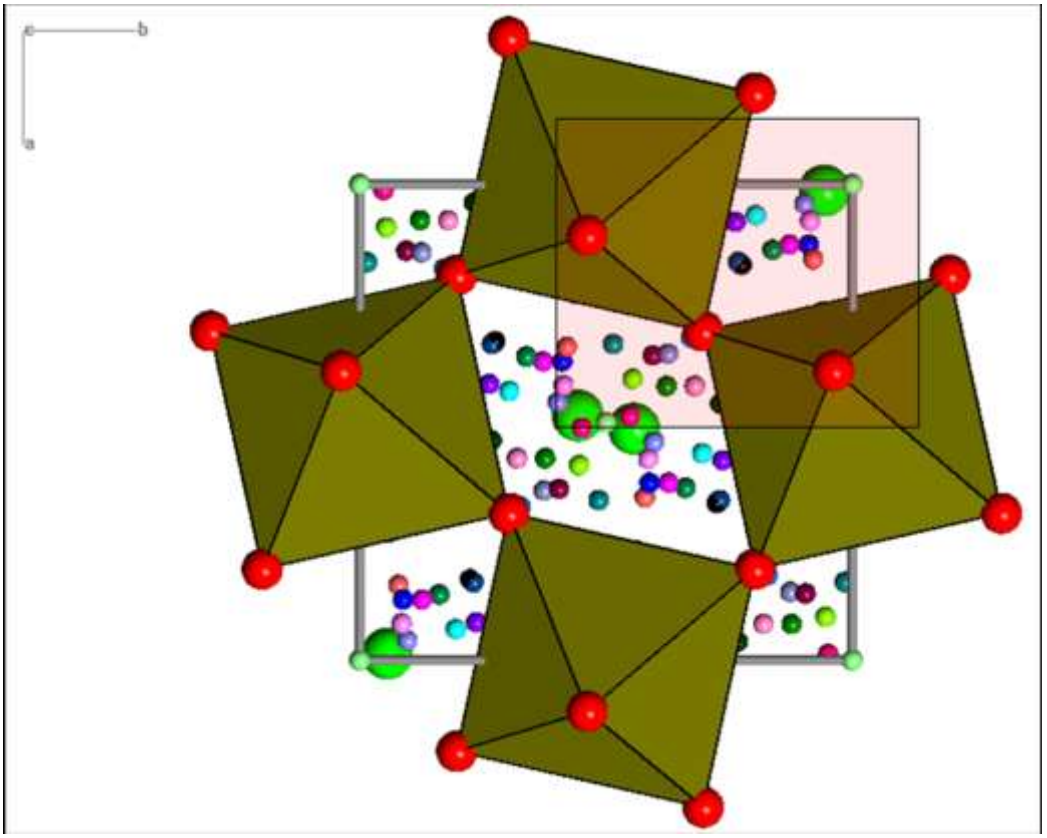

Figure 6.4.a. Projection onto the (001) plane of the structure of Mg-perovskite at P = 40 GPa with the related bond, ring and cage critical points. The selected rectangle is enlarged in figure 6.4.b

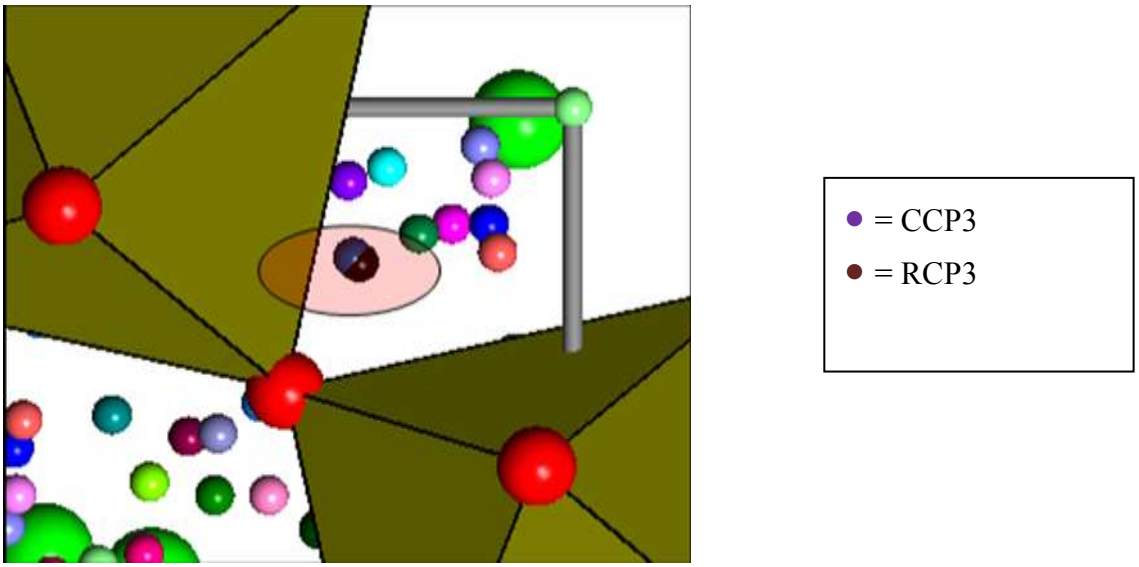

Figure 6.4.b. Enlargement of the rectangle selected in the figure 6.4.a.

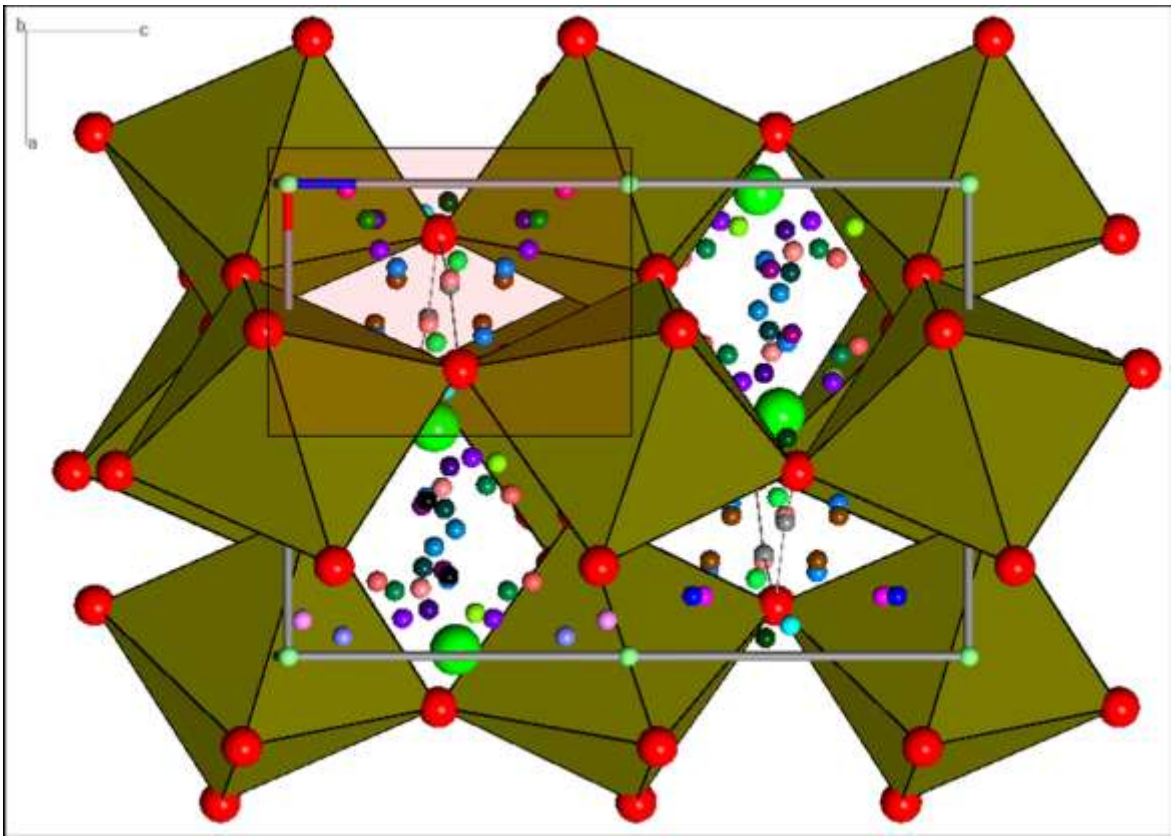

Fig. 6.5.a Perspective view onto the $(0\bar{1}0)$ plane of the structure of Mg-perovskite at P = 40 GPa with the related bond, ring and cage critical points. The selected rectangle is enlarged in figure 6.5.b.

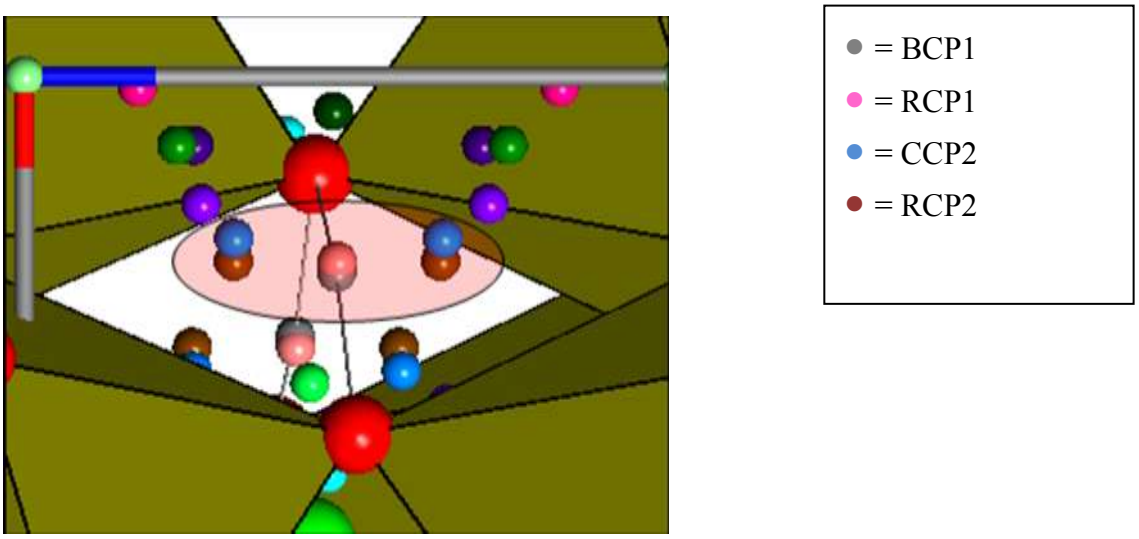

Figure 6.5.b. Enlargement of the rectangle selected in the figure 6.5.a.

It is worth to note that the emergence of the CCP3-RCP3 couples corresponds to the pressure value where the post-spinel transition occurs. Therefore it seems to indicate the passage between the stability field of the ringwoodite phase to that of the perovskite phase. A further increase of the pressure determines an increase of the distance CCP3-RCP3 and the simultaneous decrease of the distance CCP2-RCP2, while, again, the distance BCP1-RCP1 is quite unaltered (Figure 6.6-6.7).

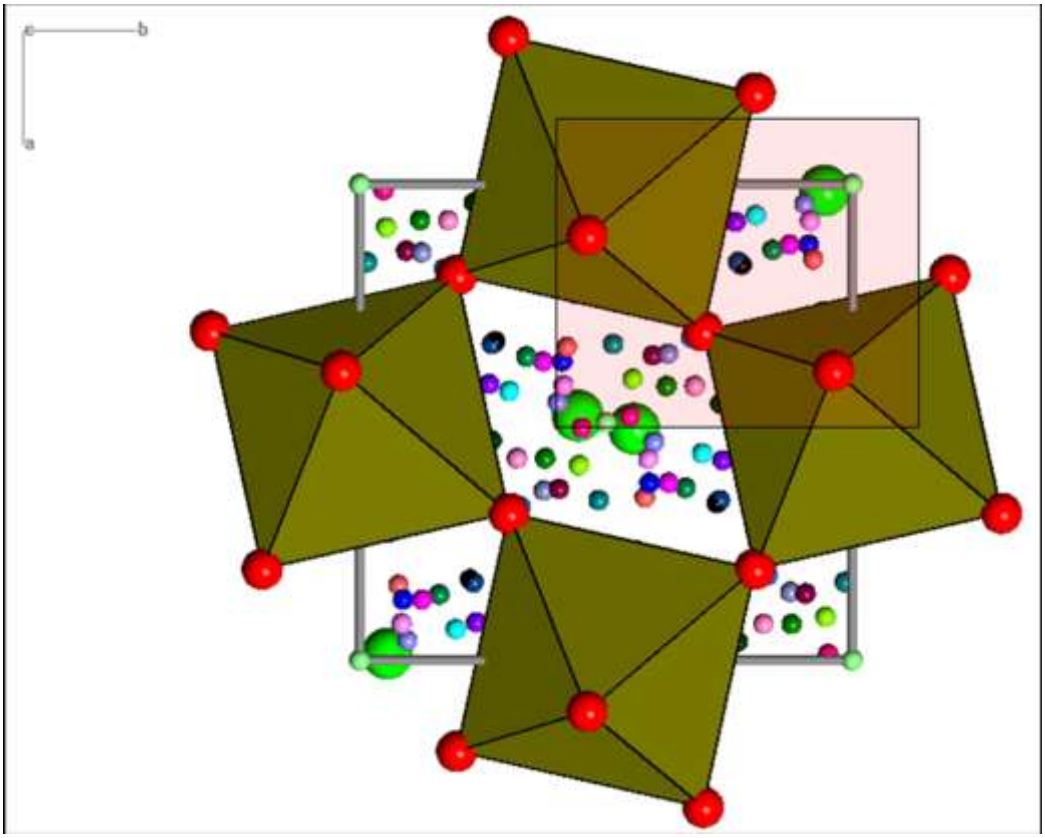

Fig.6.6.a Projection onto the (001) plane of the structure of Mg-perovskite at P = 53 GPa with the related bond, ring and cage critical points. The selected rectangle is enlarged in figure 6.6.b.

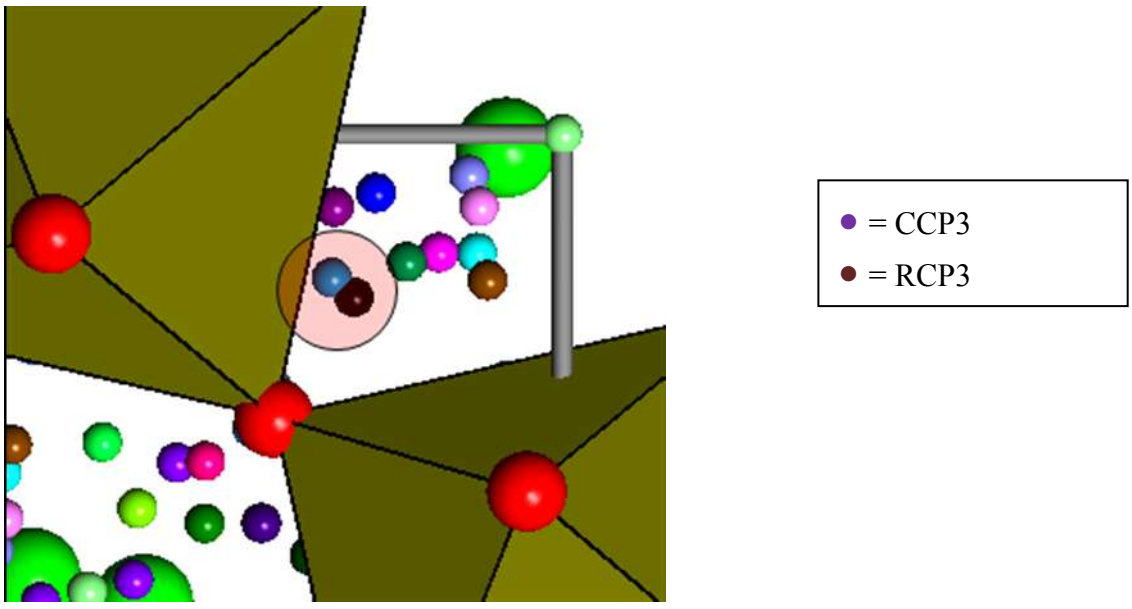

Figure 6.6.b. Enlargement of the rectangle selected in the figure 6.4.a.

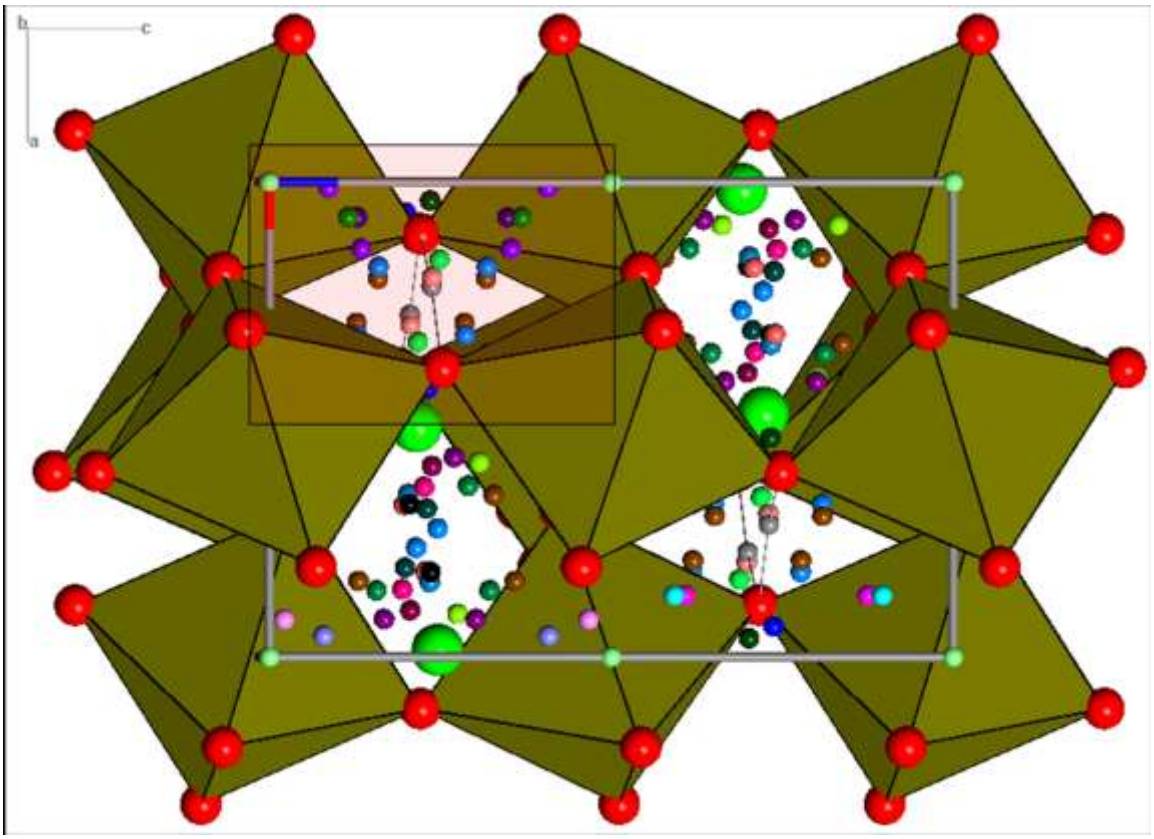

Fig. 6.7.a Perspective view onto the $(0\bar{1}0)$ plane of the structure of Mg-perovskite at P = 53 GPa
with the related bond, ring and cage critical points. The selected rectangle is enlarged in figure 6.7.b.

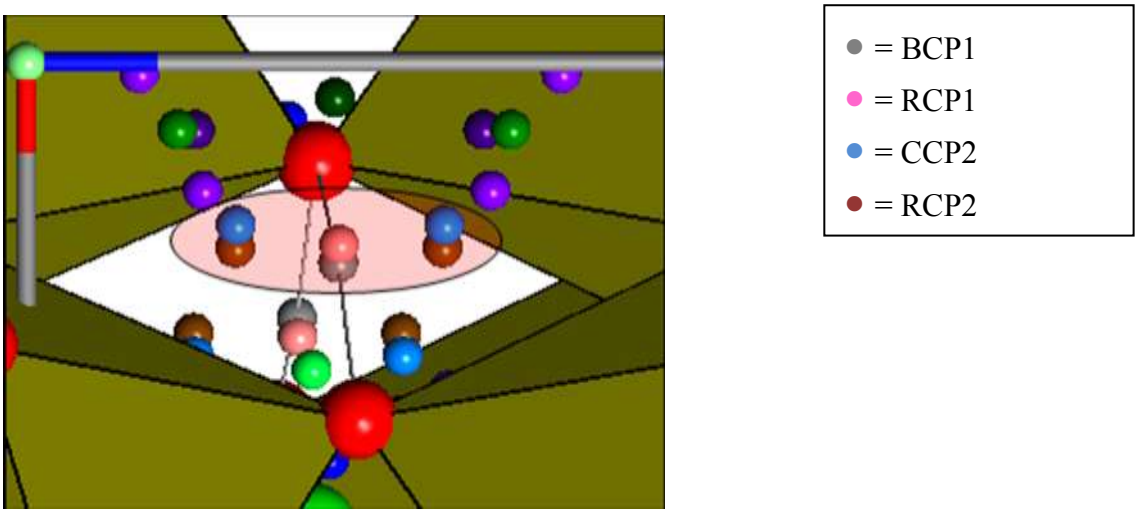

Figure 6.7.b. Enlargement of the rectangle selected in the figure 6.7.a.

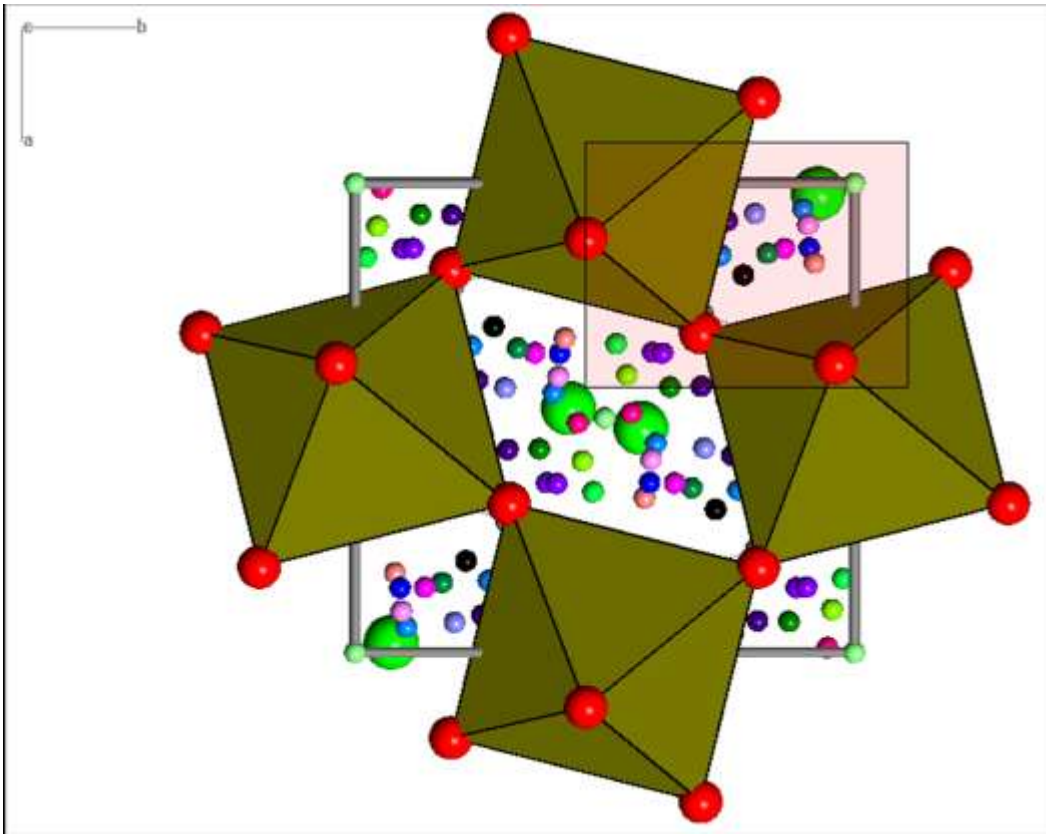

Fig.6.8.a Projection onto the (001) plane of the structure of Mg-perovskite at P = 135 GPa with the related bond, ring and cage critical points. The selected rectangle is enlarged in figure 6.8.b.

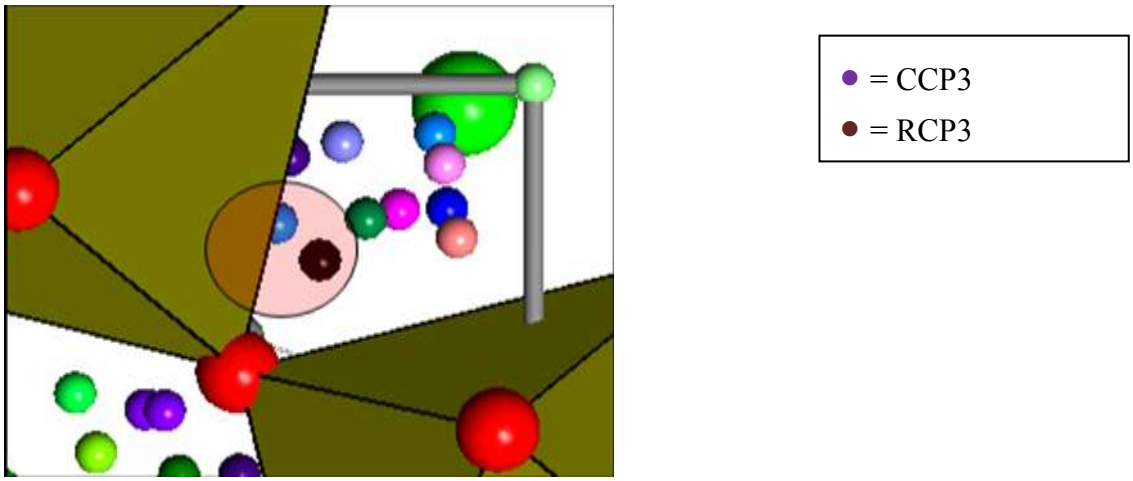

Figure 6.8.b. Enlargement of the rectangle selected in the figure 6.8.a.

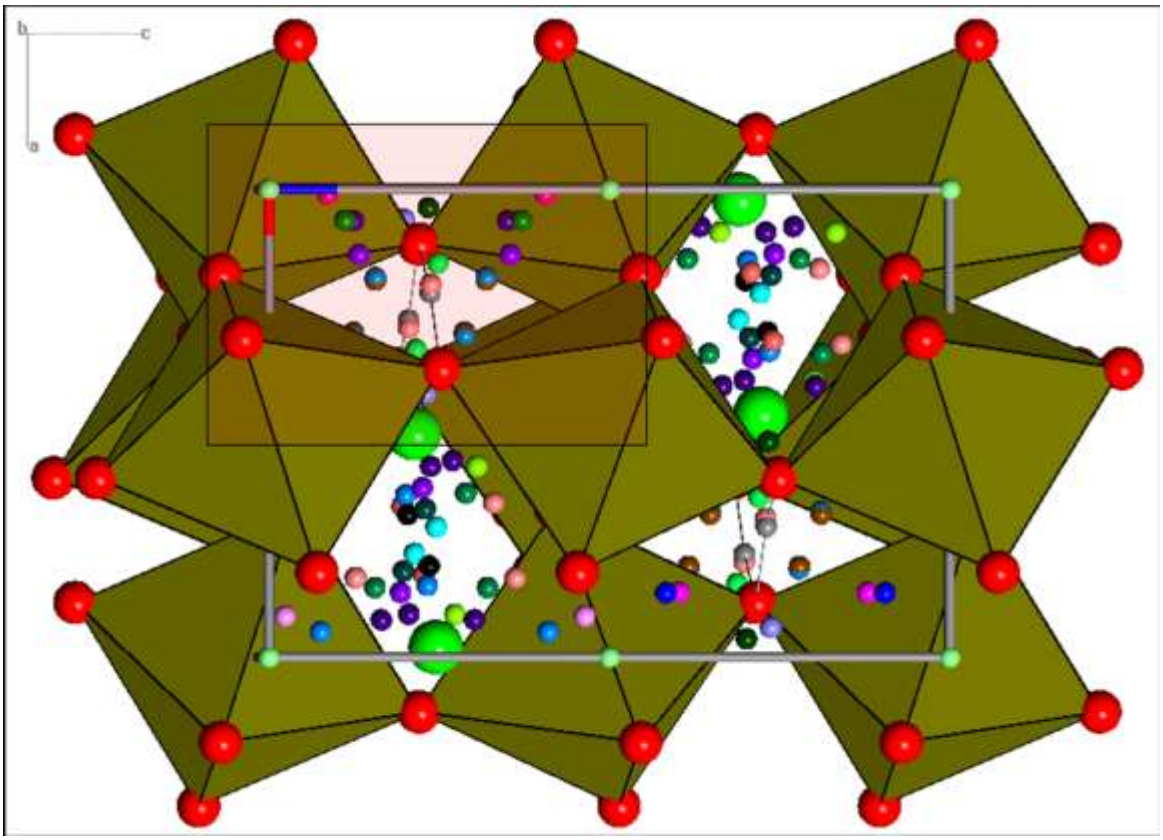

Fig. 6.9.a Perspective view onto the $(0\bar{1}0)$ plane of the structure of Mg-perovskite at P = 135 GPa with the related bond, ring and cage critical points. The selected rectangle is enlarged in figure 6.8.b.

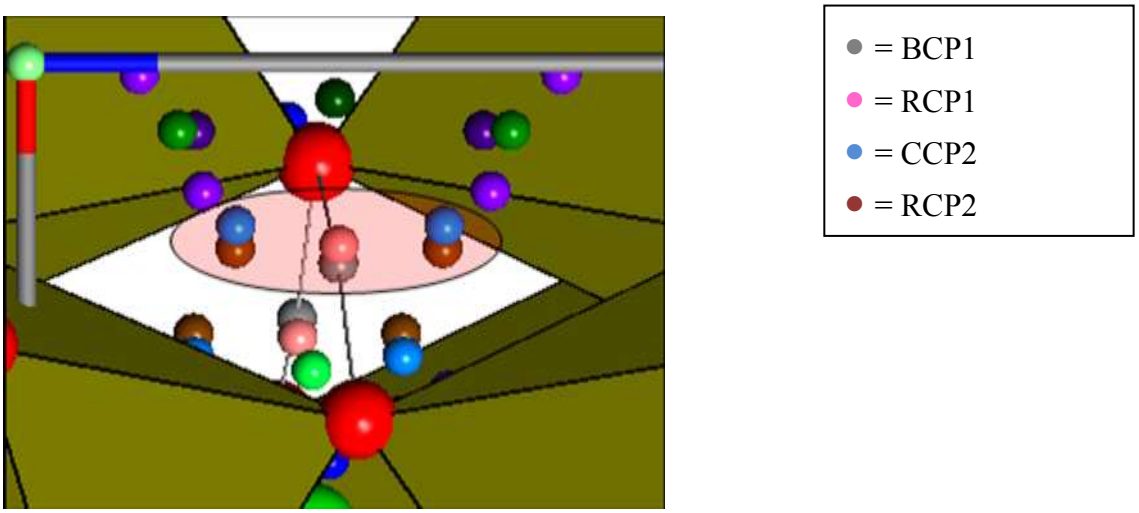

Figure 6.9.b. Enlargement of the rectangle selected in the figure 6.8.a.

Finally, in the following pictures the topological features corresponding to very high pressure values are reported. Intriguingly, it has been observed the disappearance of the CCP2-RCP2 couple. At the same time, it has been observed that the BCP1-RCP1 distance start to slight decrease.

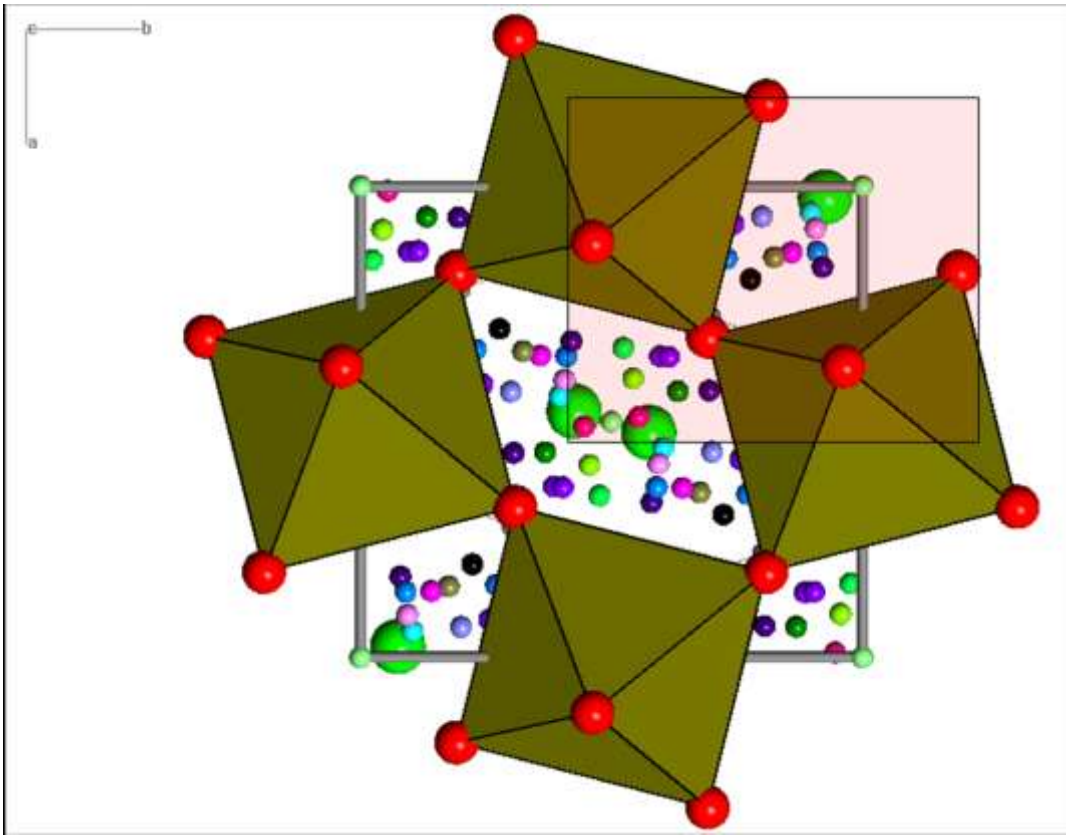

Fig.6.10.a Projection onto the (001) plane of the structure of Mg-perovskite at P = 53 GPa with the related bond, ring and cage critical points. The selected rectangle is enlarged in figure 6.6.b.

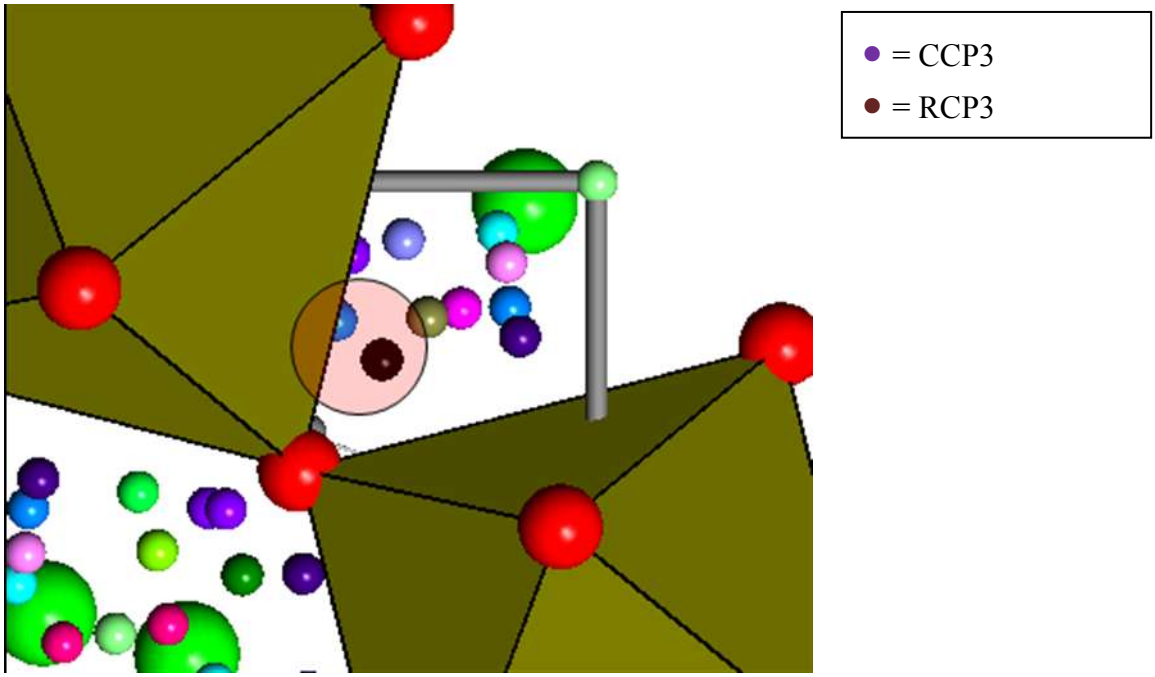

Figure 6.10.b. Enlargement of the rectangle selected in the figure 6.4.a.

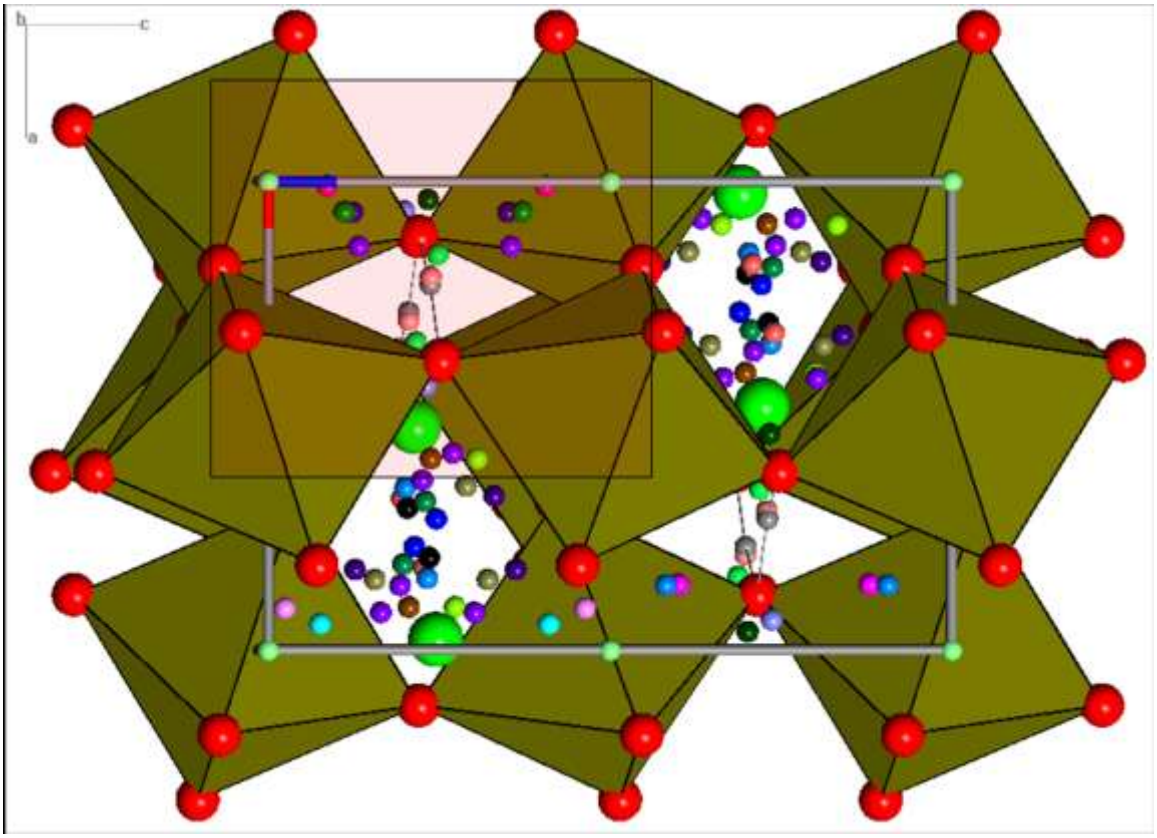

Fig. 6.11.a Perspective view onto the $(0\bar{1}0)$ plane of the structure of Mg-perovskite at P = 53 GPa with the related bond, ring and cage critical points. The selected rectangle is enlarged in figure 6.7.b.

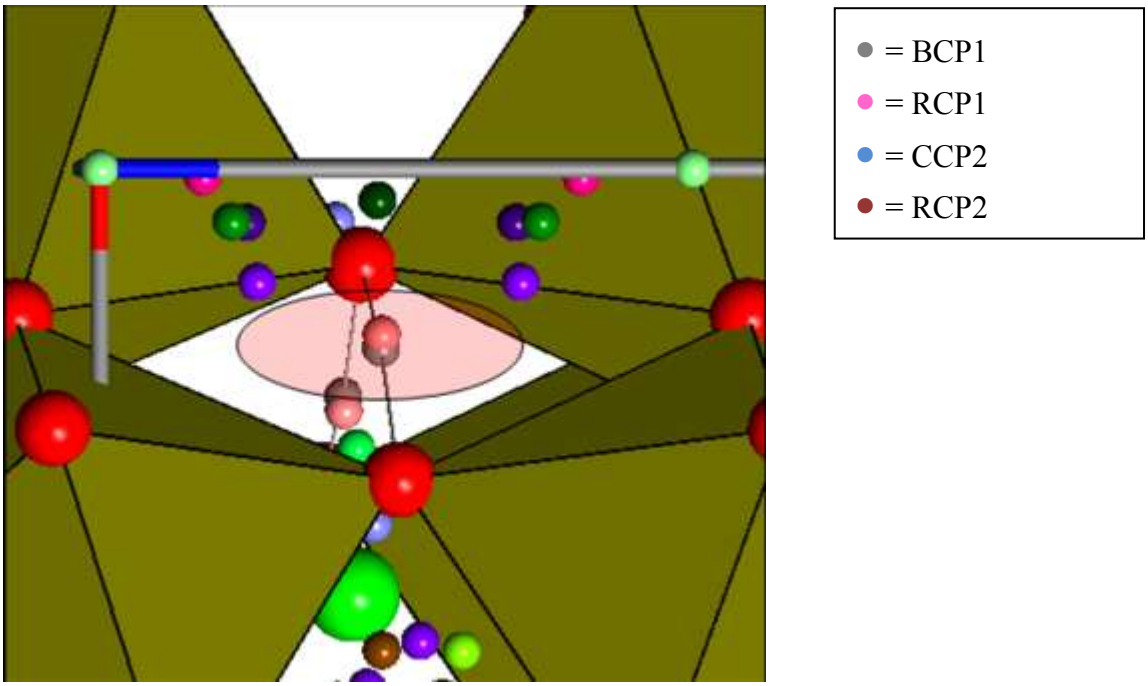

Figure 6.11.b. Enlargement of the rectangle selected in the figure 6.7.a.

.It is interesting to underline that the pressure where the disappearance of the RCP2-RCP3 couple occurs is ~ 130 GPa which correspond to the pressure where the perovskite to post-perovskite phase transition takes place.

The most important topological results are summarized in the following figures where the distances between the three critical points couples are reported:

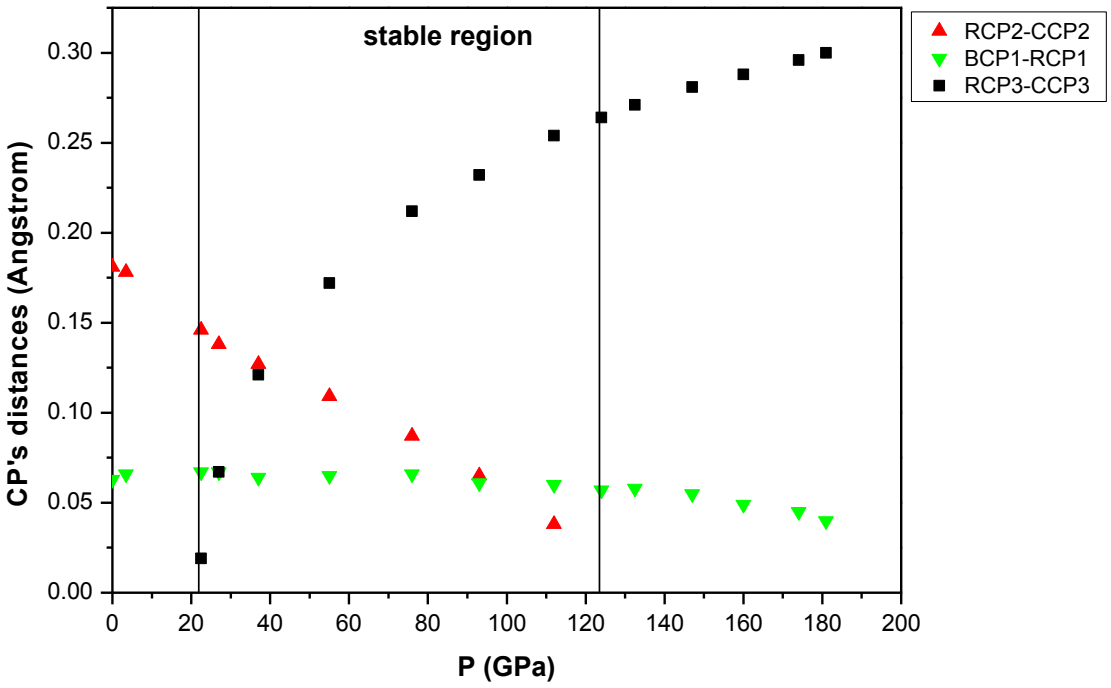

Figure 12. Plot of the distances between the three couples of coalescent critical points as a function of the pressure.

Perusal of Figure 12 illustrates how the Bader's topological analysis provides an effective tool for the delineation of the stability field of the mineralogical phases. The first topological anomaly, i.e. the emergence of the CCP3-RCP3 couple at ~22 GPa, is a clear indication of the stabilization of the perovskite phase, while the inverse process observed at ~124 GPa, i.e. the vanishing of the CCP2-RCP2, indicates the destabilization of this phase. Since the two observed phase transitions involve the coalescence of two critical points, they can be interpreted in the light of the catastrophe theory as fold catastrophes.

It is worth to underline the important geophysical implication of these results. In particular, the second observed fold catastrophe occurs at a pressure value that correspond at ~2600 Km depth, exactly to the "*D"-layer*" a 100-300 km thick layer lying just above the core-

mantle boundary, under a pressure of ~120 to 135 GPa. In this region, seismic observations provide evidence of heterogeneities in wave propagation and sound velocities.

In various works the perovskite to post-perovskite phase transition, that occurs at this pressures, is invoked as the reason for this heterogeneities.

Chapter 7

Conclusions and outlook

An approach based of the Bader's topological analysis of the ab-initio computed electron density has been successfully applied to the characterization of two mineralogical phases, namely the ringwoodite and the Mg-perovskite, under high pressure conditions.

The main results of this study are briefly summarized in the following. First of all, first principles calculations showed that the ringwoodite phase, at high pressures, becomes thermodynamically unfavorable in comparison with Mg-perovskite and periclase. A detailed topological analysis of the ringwoodite has been afforded for the first time providing important topological evidences of the approach of the phase transition and indicating the central role played from the oxygen atoms in the pressure induced phase transition. In particular, the GR(0) value, that reflects the distortion of the $\nabla\rho$ field of the charge density caused by the formation of chemical bond, for the oxygen atom reaches the value -3N at ~32.9 GPa. This situation is indicative of a certain tendency of the atom to break the bonds with the neighboring atoms. Furthermore, the investigation of the structural stability in terms of the Catastrophe theory showed a non-transversal intersection between the stable and the unstable manifolds of two bond critical points, revealing the occurrence of a *conflict catastrophe mechanism* induced by pressure at around 30 GPa.

Concerning the Mg-perovskite phase, the occurrence of two *fold catastrophe mechanisms* has been observed. The first, observed at ~22 GPa, consists in the emergence of a CCP/RCP couple and it is a clear indication of the stabilization of the perovskite phase. This result perfectly agrees with the seismic discontinuity at 660 Km between the mantle transition zone and the lower mantle. The second, at ~124 GPa, is due to the progressive

approach of a second CCP/RCP couple, until the coalescence is reached at the transition point. This result is a clear confirmation of the transition from the Mg-perovskite phase to the so-called post-perovskite phase which, as already mentioned, is responsible of the discontinuity in seismic velocities observed above the core–mantle boundary (the D" layer). Moreover, perusal of the GR(0) values indicates a strong distortion of the $\nabla\rho$ field, and therefore a strong binding of the oxygen atoms in the crystalline structure, in the whole pressure range.

The proposed approach proved to be a useful method for the investigation and the prediction of phase changes or phase breakdowns occurring under conditions at which laboratory experiments are extremely difficult, such as those of the lower mantle phases.

References

Bader RFW (1991) A quantum theory of molecular structure and its applications. Chemical Reviews 91: 893–928

Bader RFW (1994) Atoms in molecules. International series of monographs in chemistry. vol 22. Oxford University Press, Oxford, UK

Becke AD (1993) Density-functional thermochemistry III. The role of exact exchange. J Chem Phys 98: 5648–5652

Becke AD (1988) Density-functional exchange-energy approximation with correct asymptotic behavior. Phys Rev A 38: 3098–3100

Christensen UR & Yuen DA (1985) Layered convection induced by phase transitions. J Geophys Res 90: 10291–10300

Chopelas A, Boehler R, Ko T (1994) Thermodynamics and behavior of γ-Mg_2SiO_4 at high pressure: Implications for Mg_2SiO_4 phase equilibrium. Phys Chem Minerals 21: 6351-359

Chudinovskikh L & Boehler R (2001) High-pressure polymorphs of olivine and the 660-km seismic discontinuity. Nature 411: 574-577

Demichelis R, Civalleri B, Ferrabone M and Dovesi R (2019). On the performance of eleven DFT functional in the description of the vibrational properties of aluminosilicates. Int. J. Quantum Chem. 110 :406.

Deschamps F and Jeannot T (2004). Towards a lower mantle reference temperature and composition. Earth. Planet. Sc. Lett. 222: 161

Deuss A, Redfern SAT, Chambers K, Woodhouse JH (2006) The nature of the 660 km discontinuity in Earth's mantle from global seismic observations of PP precursors. Science 311: 198–201

Dovesi R, Saunders VR, Roetti C, Orlando R, Zicovich-Wilson CM, Pascale F, Civalleri B, Doll K, Harrison NM, Bush IJ, D'Arco P, Llunell M (2009) CRYSTAL09 User's Manual. University of Torino, IT

Dziewonski AM & Anderson DL (1981) Preliminary reference Earth model. Phys Earth Planet Inter 25: 297–356

Frost DJ (2008) The Upper Mantle and Transition Zone. Elements 4: 171-176

Fukao Y, Obayashi M, Inoue H, Nenbai M (1992) Subducting slabs stagnant in the mantle transition zone. J Geophys Res 97: 4809–4822

Gatti C (1999) TOPOND-98 User's Manual. CNR-CSRSRC, Milano, Italy

Hama J and Suito K (2001). Thermoelastic models of minerals and the composition of the Earth's lower mantle. Phys. Earth. Planet. In. 125:147-166

Irifune T & Ringwood AE (1987) Phase transformations in primitive MORB and pyrolite compositions to 25 GPa and some geophysical implication. In: Manghnani MH, Syono Y (eds) High Pressure Research in Mineral Physics. American Geophysical Union, Washington, DC, pp 231–242

Irifune T, Nishiyama N, Kuroda K, Inoue T, Isshiki M, Utsumi W, Funakoshi K, Urakawa S, Uchida T, Katsura T, Ohtaka O (1998) The postspinel phase boundary in Mg_2SiO_4 determined by in situ X-ray diffraction. Science 279:1698–1700

Ita JJ & Stixrude L (1992) Petrology, elasticity, and composition of the mantle transition zone. J Geophys Res 97: 6849-6866

Liu L, Mernagh TP, Irifune T (1994) High pressure Raman spectra of β-Mg_2SiO_4, γ-Mg_2SiO_4, $MgSiO_3$-ilmenite and $MgSiO_3$-perovskite. J Phys Chem Solids 55: 185-193

Kiefer B, Stixrude L, Wentzcovitch R (1999) Normal and inverse ringwoodite at high pressures. Am Mineral 84: 288–293

Meng Y, Fei Y, Weidner D, Gwanmesia GD, Hu J (1994) Hydrostatic compression of γ - Mg_2SiO_4 to mantle pressures and 700 K: thermal equation of state and related thermodynamic properties. Phys Chem Miner 21: 407–412

Kleppe AK, Jephcoat AP, Smyth JR, Frost DJ (2002) On protons, iron and the high-pressure behavior of ringwoodite. Geophys Res Lett 29: 1-4

Kleppe AK, Jephcoat AP, Smith JR (2002) Raman spectroscopic study of hydrous γ-Mg_2SiO_4 to 56GPa. Phys Chem Minerals 29: 473-476

Kubo T, Ohtani E, Kato T, Urakawa S, Suzuki A, Kanbe Y, Funakoshi K, Utsumi W, Kikegawa T, Fujino K (2002) Mechanism and kinetics of the post-spinel transformation in Mg_2SiO_4. Phys Earth Plan Int 129: 153-171

Kubo T, Kaneshima S, Torii Y, Yoshioka S (2009) Seismological and experimental constraints on metastable phase transformations and rheology of the Mariana slab. Earth and Planet Sci Lett 287: 12–23

Lee C, Yang W, Parr RG (1988) Development of the Colle-Salvetti correlation-energy formula into a functional of the electron density. Phys Rev B 37: 785–789

Liu L, Lin C-C, Mernagh TP, Inoue T (2002) Raman Spectra of hydrous γ-Mg_2SiO_4 at various pressures and temperatures. Phys Chem Minerals 29: 181-187

Merli M, Nestola F, Sciascia L (2011) Bader's analysis of the electron density in the Pbca enstatite – Pbcn protoenstatite phase transition. Eur J Mineral 23: 197–205

Navrotsky A (1994) Physics and Chemistry of Earth Materials. Cambridge University Press, Cambridge, UK

Nada R, Nicholas JB, McCarthy MI, Hess AC (1996) Basis sets for ab initio periodic Hartree-Fock studies of zeolite/adsorbate interactions: He, Ne, and Ar in silica sodalite. Int J Quant Chem 60: 809-820

Oganov AR, Price GD (2005). Ab-initio thermodynamics of $MgSiO_3$ perovskite at high pressures and temperatures. J. Chem.Phys. 122 : 12451

Ottonello G, Civalleri B, Ganguly J, Vetuschi Zuccolini M, Noel Y (2009) Thermophysical properties of the a–b–c polymorphs of Mg_2SiO_4: a computational study. Phys Chem Minerals 36: 87–106

Palis J, Smale S (1970) Structural Stability Theorems. Proc Sympos Pure Math AMS 14: 223-232

Piekarz P, Jochym PT, Parlinski K, Lazewski J (2002) High-pressure and thermal properties of c-Mg_2SiO_4 from first-principles calculations. J Chem Phys 117:3340–3344

Poirier JP (1991) Introduction to the physics of the Earth's Interior. Cambridge University Press, Cambridge, UK , pp 214-226

Prencipe M, Scanavino I, Nestola F, Merlini M, Civalleri B, Marco B and Dovesi R (2010). High-pressure thermoelastic properties of beryl ($Al_4Be_6Si_{12}O_{36}$) from ab-initio calculations, and observations about the source of thermal expansion. Phys. Chem.Miner. 38: 223

Ringwood AE & Major A (1970) The system Mg_2SiO_4 – Fe_2SiO_4 at high pressure and temperatures. Phys Earth Planet Inter 3: 89–108

Ringwood AE (1982) Phase transformations and differentiation in subducted lithosphere: implications for mantle dynamics, basalt petrogenesis, and crustal evolution. J Geol 90: 611– 643

Ringwood AE (1991) Phase transformations and their bearing on the constitution and dynamics of the mantle. Geochim Cosmochim Acta 55: 2083- 2110

Ringwood AE (1994) Role of the transition zone and 660 km discontinuity in mantle dynamics. Phys Earth Planet Inter 86: 5–24

Saunders VR, Dovesi R, Roetti C, Orlando R, Zicovich-Wilson CM, Harrison NM, Doll K, Civalleri B, Bush LJ, D'Arco P, Llunell M (2003) CRYSTAL 2003 user's manual. University of Torino, Torino, IT

Shim S, Duffy TS, Shen G (2001) The post-spinel transformation in Mg2SiO4 and its relation to the 660-km seismic discontinuity. Nature 411: 571

Stephens PJ, Devlin FJ, Chabalowski CF, Frisch MJ (1994), Ab-initio calculation of vibrational absorption and circular dichroism using density functional force fields. J. Phys. Chem 98: 11623

Tackley RJ, Stevenson DJ, Glatzmaier GA, Schubert G (1993) Effects of an endothermic phase transition at 670 km depth in a spherical model of convection in the Earth's mantle. Nature 361: 699

Ungureanu CG, Prencipe M and Cossio R (2019). Ab-initio quantum-mechanical calculation of $CaCO_3$ aragonite at hoigh pressure : thermodynamic properties and comparison with experimental data. Eur. J. Mineral. 22 : 693

Van der Hilst R (1995) Complex morphology of subducted lithosphere in the mantle beneath the Tonga trench. Nature 374: 154–157

Towler MD, Allan NL, Harrison NM, Saunders VR, Mackrodt WC, Apra' E (1994) An ab initio Hartree-Fock study of MnO and NiO. Phys Rev B 50: 5041-5054

Valenzano L, Noel Y, Orlando R, Zicovich-Wilson CM, Ferrero M, Dovesi R (2006) Ab Initio vibrational spectra and dielectric properties of carbonates: magnesite, calcite and dolomite. Theor Chem Acc 117: 991-1000

Yamazaki D, Kato T, Ohtani E, Toriumi M (1996) Grain Growth Rates of $MgSiO_3$ Perovskite and Periclase Under Lower Mantle Conditions. Science 274: 2052-2054

Yu YG, Wentzcovitch RM (2006) Density functional study of vibrational and thermodynamic properties of ringwoodite. J Geophys Res 111:B12202

Zerr A, Reichmann H, Euler H, Boehel R (1993) Hydrostatic Compression of γ-$(Mg_{0.6},Fe_{0.4})_2SiO_4$ to 50.0 GPa. Phys Chem Minerals 19: 507-509

Wu Z and Cohen RE (2006). More accurate generalized gradient approximation for solids. Phys. Rev. B. 73: 235116

Zhao Y & Anderson DL (1994) Mineral physics constraints on the chemical composition of the Earth's lower mantle. Phys Earth Planet Inter 85: 273-292

Appendix

Crystal 09 - INPUT file

INPUT FILE	**Explanations (***Crystal09 user's manual***)**
Mg-perovskite	Title
CRYSTAL 1 0 0 P B N M 4.8099 4.9422 6.9440 4 12 -4.883E-01 -4.509E-01 2.5E-01 14 -5.000E-01 0.0E+00 -5.0E-01 8 1.0417E-01 4.6162E-01 2.5E-01 8 1.954E-01 2.011E-01 -4.458E-01	 IFLAG IFHR IFSO space group a, b, c, cell parameters (°A) non equivalent atoms Z=12, Magnesium coordinates Z=17, Silicon coordinates Z=8, Oxygen1 coordinates Z=8, Oxygen2 coordinates
OPTGEOM CVOLOPT FULLOPTG MAXCYCLE 300 MAXITACE 1000 ENDOPT END	Geometry optimization input block full geometry optimization at constant volume full geometry optimization max number of optimization steps max number of iteration cycles in atom/cell iterative optimization End of geometry optimization input block

	All electron Basis set for Silicon
14 5	Z=14, Silicon; 5 shells
0 0 8 2.0 1.0	free BS; s shell; 8 GTF; CHE=2; scale factor 1
149866.0 0.0001215	1st gauss exp; s contraction coefficient
22080.6 0.0009770	2nd gauss exp; s contraction coefficient
4817.5 0.0055181	3rd gauss exp; s contraction coefficient
1273.5 0.0252000	4th gauss exp; s contraction coefficient
385.11 0.0926563	5th gauss exp; s contraction coefficient
128.429 0.2608729	6th gauss exp; s contraction coefficient
45.4475 0.4637538	7th gauss exp; s contraction coefficient
16.2589 0.2952000	8th gauss exp; s contraction coefficient
0 1 8 8.0 1.0	free BS; sp shell; 8 GTF; CHE=8; scale factor 1
881.111 -0.0003 0.0006809	1st gauss exp; s contr. coeff; p contr. coeff
205.84 -0.0050 0.0059446	2nd gauss exp; s contr. coeff; p contr. coeff
64.8552 -0.0368 0.0312000	3rd gauss exp; s contr. coeff; p contr. coeff
23.9 -0.1079 0.1084000	4th gauss exp; s contr. coeff; p contr. coeff
10.001 0.0134 0.2378000	5th gauss exp; s contr. coeff; p contr. coeff
4.4722 0.3675 0.3560066	6th gauss exp; s contr. coeff; p contr. coeff
2.034 0.5685 0.3410000	7th gauss exp; s contr. coeff; p contr. coeff
0.9079 0.2065 0.1326000	8th gauss exp; s contr. coeff; p contr. Coeff
0 1 3 0.0 1.0	free BS; sp shell; 3 GTF; CHE=0; scale factor 1
2.6668 -0.0491 0.0465000	1st gauss exp; s contr. coeff; p contr. coeff
1.0780 -0.1167 -0.1005000	2nd gauss exp; s contr. coeff; p contr. coeff
0.3682 0.2300 -1.0329000	3rd gauss exp; s contr. coeff; p contr. Coeff
0 1 1 0.0 1.0	free BS; sp shell; 1 GTF; CHE=0; scale factor 1
0.193 1.0 1.0	gauss exp; s contr. coeff; p contr. Coeff
0 3 1 0. 1.	free BS; d shell; 1 GTF; CHE=0; scale factor 1
0.566 1.0	gauss exp; s contraction coefficient

12 5	Z=12, Magnesium; 5 shells
0 0 8 2.0 1.0	free BS; s shell; 8 GTF; CHE=2; scale factor 1
68370.0 0.0002226	1st gauss exp; s contraction coefficient
9661.0 0.001901	2nd gauss exp; s contraction coefficient
2041.0 0.011042	3rd gauss exp; s contraction coefficient
529.6 0.05005	4th gauss exp; s contraction coefficient
159.17 0.1690	5th gauss exp; s contraction coefficient
54.71 0.36695	6th gauss exp; s contraction coefficient
21.236 0.4008	7th gauss exp; s contraction coefficient
8.791 0.1487	8th gauss exp; s contraction coefficient
0 1 5 8.0 1.0	free BS; sp shell; 5 GTF; CHE=8; scale factor 1
143.7 -0.00671 0.00807	1st gauss exp; s contr. coeff; p contr. coeff
31.27 -0.07927 0.06401	2nd gauss exp; s contr. coeff; p contr. coeff
9.661 -0.08088 0.2092	3rd gauss exp; s contr. coeff; p contr. coeff
3.726 0.2947 0.3460	4th gauss exp; s contr. coeff; p contr. coeff
1.598 0.5714 0.3731	5th gauss exp; s contr. coeff; p contr. coeff
0 1 1 0.0 1.0	free BS; sp shell; 1 GTF; CHE=0; scale factor 1
0.688 1.0 1.0	gauss exp; s contr. coeff; p contr. Coeff
0 1 1 0.0 1.0	free BS; sp shell; 1 GTF; CHE=0; scale factor 1
0.28 1.0 1.0	gauss exp; s contr. coeff; p contr. Coeff
0 3 1 0. 1.	free BS; d shell; 1 GTF; CHE=0; scale factor 1
0.650 1.	gauss exp; s contraction coefficient

8 4	Z=8, Oxygen; 4 shells
0 0 8 2.0 1.0	free BS; s shell; 8 GTF; CHE=2; scale factor 1
8020.0 0.00108	1st gauss exp; s contraction coefficient
1338.0 0.00804	2nd gauss exp; s contraction coefficient
255.4 0.05324	3rd gauss exp; s contraction coefficient
69.22 0.1681	4th gauss exp; s contraction coefficient
23.90 0.3581	5th gauss exp; s contraction coefficient
9.264 0.3855	6th gauss exp; s contraction coefficient
3.851 0.1468	7th gauss exp; s contraction coefficient
1.212 0.0728	8th gauss exp; s contraction coefficient
0 1 4 8.0 1.0	free BS; sp shell; 4 GTF; CHE=8; scale factor 1
49.43 -0.00883 0.00958	1st gauss exp; s contr. coeff; p contr. Coeff
10.47 -0.0915 0.0696	2nd gauss exp; s contr. coeff; p contr. coeff
3.235 -0.0402 0.2065	3rd gauss exp; s contr. coeff; p contr. coeff
1.217 0.379 0.347	4th gauss exp; s contr. coeff; p contr. coeff
0 1 1 0.0 1.0	free BS; sp shell; 1 GTF; CHE=0; scale factor 1
0.4764 1.0 1.0	gauss exp; s contr. coeff; p contr. Coeff
0 1 1 0.0 1.0	free BS; sp shell; 1 GTF; CHE=0; scale factor 1
0.170 1.0 1.0	gauss exp; s contr. coeff; p contr. Coeff
99 0	The basis set input ends
CHARGED	allows non-neutral cell
END	close Basis Set input block
FIXINDEX	Reference geometry to classify integrals
SCFDIR	In the SCF step monoelectronic and bielectronic integrals are evaluated at each cycle. No screening of the integrals is performed.
TOLINTEG 8 8 8 8 16	Truncation criteria for bielectronic integrals
SHRINK 6 6	Shrinking factor in reciprocal space; Shrinking factor for a denser k point net (Gilat net) in the evaluation of the Fermi energy and density matrix
DFT	DFT Hamiltonian

EXCHANGE	exchange functional
WCGGA	GGA - Wu-Cohen
CORRELAT	Correlation Potential
LYP	GGA. Lee-Yang-Parr
HYBRID 16	Hybrid HF-DFT functionals Part of the exact Hartree-Fock exchange into the Exchange functional. 16% mixing of exact Hartree-Fock and DFT exchange can be used.
XXLGRID	”extra extra large” predefined grid
END	
LEVSHIFT 2 0	a level shifter 0.2 hartree
EXCHSIZE 3685032	size of exchange bipolar expansion buffer
BIPOSIZE 1630800	size of coulomb bipolar expansion buffer
MAXCYCLE 3000	max number of optimization steps
FMIXING 20	permits to mix the Fock/KS matrix derivatives between CPHF-SCF1 cycles n and n- 1 percentage of cycle n – 1
TOLDEE 7	Convergence on total Energy $1*10^{-7}$
END	
GEOM	restart with new geometrical parameters
CRYSTAL 1 0 0 P B N M 4.60189 4.77191 6.64829 4 12 -0.48548 -0.44158 0.250000	 IFLAG IFHR IFSO space group a b c cell parameters (°A) non equivalent atoms Z=12, Magnesium coordinates

14 5.000E-01 0.00E+00 -5.000E-01	Z=17, Silicon coordinates
8 0.1091 0.4620 0.25000	Z=8, Oxygen1 coordinates
8 0.1908 0.1973 -0.4438	Z=8, Oxygen2 coordinates
END	

TOPOND - INPUT file

INPUT FILE	**Explanations (*TOPOND manual*)**
CRYSTAL	
TRHO	Topological analysis of ρ (electron density)
3	Variable: IAUTO=3 Grid search in the asymmetric unit
0,1,1,0,15,12,6.	**1st variable:** IMETH=0 Newton-Raphson (NR) algorithm used in the CP search. **2nd variable:** IEXT=1 Properties (kinetic energy densities, virial density, ELF) depending on the non-diagonal elements of the first-order density matrix are also evaluated at each unique CP. **3rd variable:** IBPAT=1 Atomic Interaction Line lengths and termini are evaluated numerically for each unique (3,-1) CP. **4th variable:** IPRINT=0 normal printing. **5th variable:** NSTEP=15 max. number of Newton-Raphson (NR) algorithm steps performed in each search. **6th variable:** NNB=12 (3,-1) CPs are searched among all the unique pairs generated from a set of nuclei. The set is generated by constructing clusters of atoms around each non-equivalent atom (NEA) of the unit cell. NNB is the number of stars of neighbors used in the cluster construction around each NEA. NNB is also used in the nearest neighbor analysis around each unique CP (of any kind) found. **7th variable:** RMAX=6 maximum radius of each generated cluster (see NNB explanation). RMAX may, locally, reduce the actual value of NNB.
0.0 1.0 0.01	**1st varible:** XMI=0 Fractional coordinate intervals (fractionary units) minimum value of X **2nd variable:** XMA=1 maximum value of X **3rd variable:** XINC=0.01 grid interval along X
0.0 1.0 0.01	**1st varible:** YMI=0 Fractional coordinate intervals (fractionary units) minimum value of Y **2nd variable:** YMA=1 maximum value of Y **3rd variable:** YINC=0.01 grid interval along Y
0.0 1.0 0.01	**1st variable:** ZMI=0 Fractional coordinate intervals (fractionary units) minimum value of Z **2nd variable:** ZMA=1 maximum value of Z **3rd variable:** ZINC=0.01 grid interval along Z
1	**Variable:** NCONS number of constraints, if any, among the values of the x,y,z fractional coordinates
1 1.0	**1st variable:** conventional number of constraint type. ICO=1 Constraint type: X ≤ ay **2nd variable:** value of a in constraint ICO. ACO=1 Constraint type: X ≤ ay
END	

Index